communications earth & environment

ARTICLE

https://doi.org/10.1038/s43247-023-01034-7 OPEN

Low-frequency orbital variations controlled climatic and environmental cycles, amplitudes, and trends in northeast Africa during the Plio-Pleistocene

Rachel Lupien [1,2,3]✉, Kevin Uno[2,3], Cassaundra Rose[4], Nicole deRoberts[2], Cole Hazan[2], Peter de Menocal[5] & Pratigya Polissar[6]

The eastern Mediterranean sapropels, paced by insolation, provide a unique archive of African monsoon strength over the Late Neogene. However, the longer-term climate of this region lacks characterization within the context of changes in ice volume, sea surface temperature gradients, and terrestrial ecosystems. Here, we examine C_{28} *n*-alkanoic acid leaf wax hydrogen and carbon isotopes in sapropels, sourced from northeast Africa, along with vegetation-corrected precipitation isotopes, derived from astronomically dated sediment cores from ODP 160 Sites 966 and 967 since 4.5 million years ago. Despite sampling only wet-phase sapropels for African monsoon variability, we find a larger range in hydrogen isotopes than previously published data across wet-dry precession cycles, indicating the importance of long-term modulation of Green Sahara phases throughout the Neogene. An influence of orbital properties on regional monsoonal hydroclimate is observed, controlling up to 50% of total hydrogen isotope variance, but large changes outside of these typical frequencies account for at least 50% of the total variance. This secular trend may track changes in ice volume, tropical sea surface temperature, sea surface temperature gradients, or even lower-frequency orbital cycles. Long-term hydroclimate and environmental shifts provide new contexts for milestone events in northeast African hominin dispersal and evolution.

[1] Department of Geoscience, Aarhus University, Aarhus, Denmark. [2] Lamont-Doherty Earth Observatory, Columbia University, Palisades, CA, USA. [3] Department of Human Evolutionary Biology, Harvard University, Cambridge, MA, USA. [4] United States Climate Alliance, Augusta, ME, USA. [5] Woods Hole Oceanographic Institution, Woods Hole, MA, USA. [6] Department of Ocean Sciences, University of California, Santa Cruz, Santa Cruz, CA, USA. ✉email: rachel.lupien@geo.au.dk

The climate and environment of Africa have fluctuated substantially over the Pliocene and Pleistocene, drastically altering the landscape where our early human ancestors lived, moved, and evolved. Northeast Africa has served as the terrestrial pathway for migration from the African continent to the rest of the world, particularly during Green Sahara intervals, which allowed for movement across this otherwise barrier-like desert. Global, regional, and local processes have been shown to contribute to the patterns of climate variability near this region in Africa by way of glacial-interglacial cycling[1], monsoon precipitation[2], and land surface feedbacks[3]. Records of terrestrial climate processes in northeast Africa are central for contextualizing the environments of our hominin ancestors.

Quantitative, high-resolution records of late Pleistocene climate and environmental change highlight northeast Africa as a potential pathway for *Homo sapiens to disperse out of Africa*[4]. Other paleoclimate records from this same time interval in the eastern Africa region suggest that periods of specific climate conditions are particularly suited for hominin stability and dispersal[5]. Comprehensive modeling efforts link periods of high-amplitude, orbitally driven temperature, rainfall, and primary productivity changes to hominin dispersal[6], supporting evolutionary hypotheses that focus on orbitally driven climate drivers, such as the *variability selection hypothesis*[7,8]. Reconstructions of the climate and ecosystem change in this region are needed for disentangling the various influences and potential processes involved. However, climate and environmental variability and trends have been difficult to quantify over long time intervals due to the lack of continuous, geochemical proxy records measured in long, well-dated archives.

New quantitative reconstructions are required to assess patterns of trend, amplitude, and periodicity in order to disentangle potential climate drivers. Geochemical reconstructions from well-dated sediment cores allow for continuous measurement, which is ideal for the application of time series analysis to tease apart these patterns. Leaf wax records from both marine[4,9] and lacustrine[10,11] sediment cores document mixed signals with features of both glacial-interglacial cycles and the regional monsoon system in the late Pleistocene, highlighting the need for wider application of these approaches. Prior to the late Pleistocene, leaf wax hydrogen (δD_{wax}) and carbon ($\delta^{13}C_{wax}$) isotope records have also shown direct evidence for the eccentricity-modulation of precession cycles[10,12]. While monsoon strength has been shown to dominate the orbital-scale variability of the earlier Plio-Pleistocene[10–14], these terrestrial records are often too short to be able to reconstruct climate variability over millions of years and thus capture long-term trends and a wide range of variability frequencies. Further, near-tropical, terrestrial (including lacustrine) sediment cores are often very difficult to date, limiting the application of advanced spectral analyses to decipher periodicities and climate drivers. Recent compilations of terrestrial climate records have extended this view and highlighted the importance of the 400-kyr eccentricity cycle, but the standardization of the included records limits the temporal resolution and, thus, the range of studied frequencies[15].

To characterize the climate and environment during monsoon maxima of this region central for hominin evolution and dispersal, we present records of precipitation and vegetation from leaf wax biomarkers preserved in sapropel layers from two adjacent Mediterranean Sea sediment cores (Fig. 1) that together span the last 4.5 million years. The sapropel layering is astronomically tuned, thus providing a long, continuous, precisely dated archive from which to reconstruct climate over the Plio-Pleistocene, while geochemical tracers from terrestrial northeast Africa preserved in the cores allow for the quantification of trends, amplitudes, and spectral properties of climate and environmental change. These novel records, along with comparisons to higher-resolution X-ray fluorescence (XRF) analyses and indices, such as the Wet-Dry Index[16], will address questions of climate drivers and hominin migration through the Plio-Pleistocene.

Background

Seasonal monsoon strength fluctuation is driven by the changing distribution of solar radiation, or insolation, linked to the wobble, or precession, of Earth's orbit. Orbital precession drives temperature and pressure gradient differences between ocean and land, strengthening and weakening the monsoon system over 21 kyr cycles. Eccentricity, or the degree of circularity of Earth's orbit around the sun, varies on 100 kyr and 400 kyr cycles and modulates the amplitude of precession variability at a given latitude, but has little effect on total insolation. Obliquity, the tilt of the axis of the Earth, modulates the seasonal distribution and latitudinal gradient of insolation, and is thought to mainly contribute to climate variation at the polar regions. These orbital parameters contribute to the varying strength of the seasonal monsoon system, which can, in turn, drive changes in vegetation and terrestrial ecosystems[10, 12,17,18].

On the other hand, global climate during the Plio-Pleistocene is characterized by the gradual strengthening of the glacial-interglacial cycles[19–21]. The cooling trend is thought to trigger changes in the amplitude of the oscillations, as well as changes in the periodicity of the cycles from precession- to obliquity- to eccentricity-paced during this time[19,22]. The benthic foraminiferal oxygen isotope stack[19] documents these deep-water temperature and ice volume patterns, but the characteristic Plio-Pleistocene cycles have far-reaching effects in the climate system. Ice volume has been shown to correspond with ocean circulation, atmospheric CO_2, temperature, and sea surface temperature gradients, all of which may influence the climate conditions and ecosystems of continental Africa[23,24].

Canonical records of terrestrial African paleoclimate, such as the soil carbonate carbon and oxygen isotope compilations of eastern Africa[25], document gradual trends towards more open, arid environments. However, these outcrop measurements often represent very fine temporal and spatial scales due to the formation processes, so while it is possible to resolve long-term trends by compiling many individual measurements, analyses of temporal variability are limited. Other evidence of high latitude processes driving long-term trends in African climate, such as pollen[26] and leaf waxes[27,28], have been documented in low-resolution reconstructions from marine sediment cores off the coast of Africa, which integrate larger areas and temporal scales. Higher-resolution reconstructions from these relatively long marine sediment cores, such as dust fluxes[29,30] and other lithological proxies[16,31,32] are able to resolve the temporal scale needed for variability analyses and document the periodicity changes mimicking the Plio-Pleistocene glacial-interglacial cycles. However, recent analyses suggest the monsoon cycles do not follow the Plio-Pleistocene pattern observed in ice volume/deep sea temperature[33,34], adding to the need for further study.

There is ample evidence for regional connectivity of precipitation variability over the Plio-Pleistocene. The eastern African rift system carries evidence of synchronous, pulsed deep lake intervals across the basins that correspond to the 400 kyr eccentricity cycle[35], which is prominent in low-latitude insolation[36]. The Mediterranean sapropel layers are also a classic indicator of the wet-dry cycles that North Africa experienced over the Plio-Pleistocene. Sapropel deposition is caused by the enhanced discharge from the Nile River Delta and other North African inputs to the Mediterranean following strong monsoonal

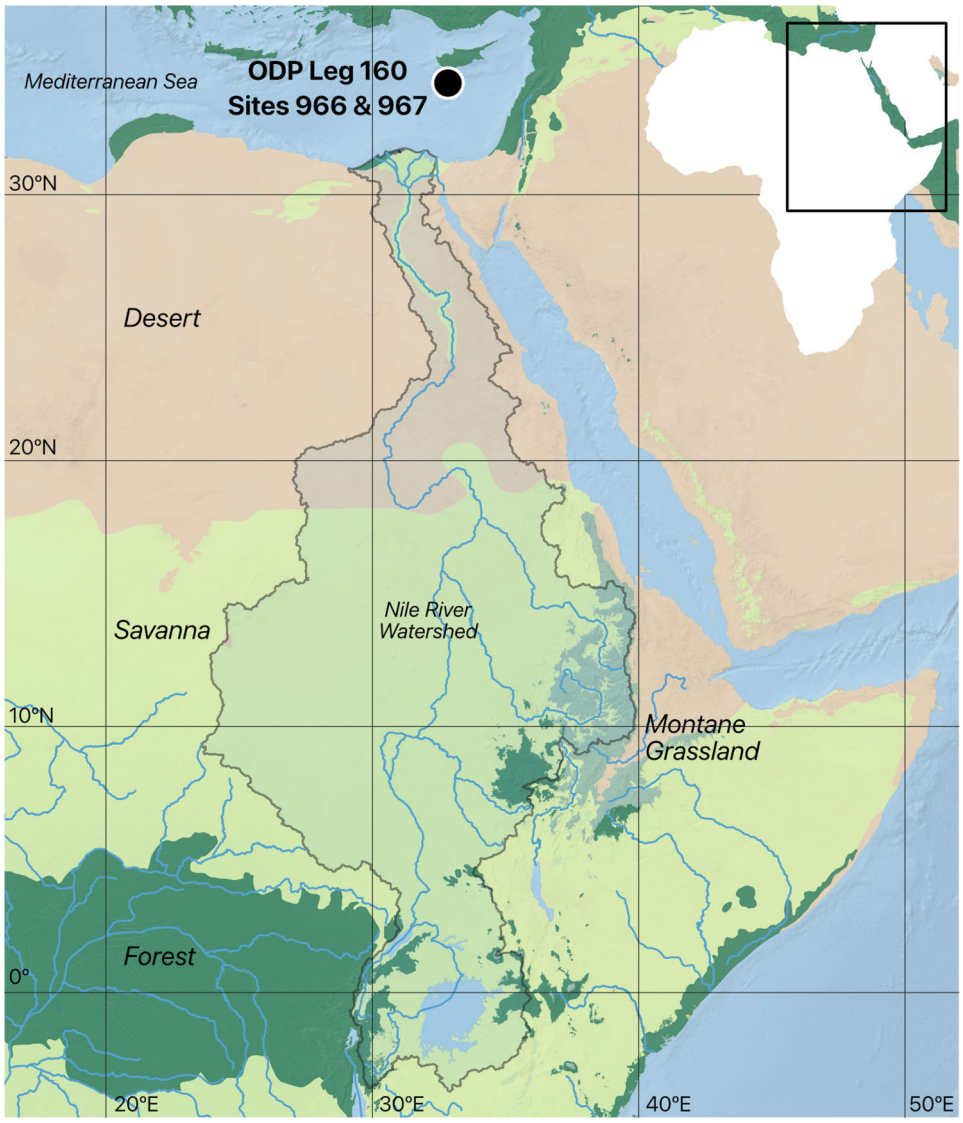

Fig. 1 Vegetation map of study location. Map of study cores from ODP Leg 160 Sites 966 and 967 in the Eastern Mediterranean with continental Northeast Africa and the fluvial component of the leaf wax shed, i.e., the Nile River watershed, highlighted in blue, with biomes[46], lakes, and rivers. Mapping software, biomes, and watershed shapefiles from opensource Quantum Geographic Information Systems (QGIS): http://qgis.osgeo.org.

rains over eastern[37,38] and western[39,40] Africa. This fresh water provides a low-density cap to the Mediterranean Sea that prevents mixing and oxygenation deep water, leading to deposition of organic-rich muds during these wet intervals. These strata have been linked to orbital precession[38,41–44] and indicate that it is highly likely that wet-dry cycles in this region were driven by both the East African Monsoon (EAM) and West African Monsoon (WAM) systems, modulated dominantly by low-latitude insolation. However, it is difficult to discern the long-term trends, as well as the amplitude of precession-band monsoon intensity in these binary (i.e., deep/shallow lake and dark/light sediment) archives.

The eastern Mediterranean Sea is bound by land masses encompassing a large range of different climate and environmental zones. Provenance studies using lignin biomarkers[14] and mineralogy[45] have indicated that a vast majority of the depositional material comes from the Nile River Valley and the northeastern Sahara Desert (Fig. 1). Leaf waxes from Northeast Africa are also likely transported by aeolian and fluvial pathways to the Mediterranean Sea, capturing the climate and environmental histories across biomes[46] covering the Ethiopian Highlands, the Nile River Valley, and the northeastern Saharan Desert when vegetated, which are seasonally affected by the EAM, and at its maximum extent, the WAM.

The eastern Mediterranean is notable for sapropel formation due to its dynamic relationship with the Nile River. These sediment layers are visually distinctive, marked by dark, organic rich muds embedded in light, nannofossil oozes. Outcrops of these strata dating back to the early Pliocene occur in Sicily and elsewhere, and sapropels are ubiquitous in deep Mediterranean Sea cores. Ocean Drilling Program (ODP) Leg 160 Sites 966 and 967[47], located on the northern margin of the Eratosthenes Seamount in the Levantine Basin (34°N, 34°E, 927 m and 2253 m water depth, respectively; Fig. 1), recovered a long record of sapropel deposition covering the past 4.5 Myr. Multiple holes at each site provide continuous composite depth scales that capture the full sapropel record (Supplementary Table 1). Due to the lack of preservation of sapropel sediment in ODP Site 967 prior to 3.2 Ma, as denoted by the Barium to Aluminum ratio (Fig. 2e), cores from both Sites 966 and 967 were necessary for leaf wax analyses.

Linking sapropel deposition to orbital cycles has been the basis of high-precision age models in the region[16,43–45]. Here, we build

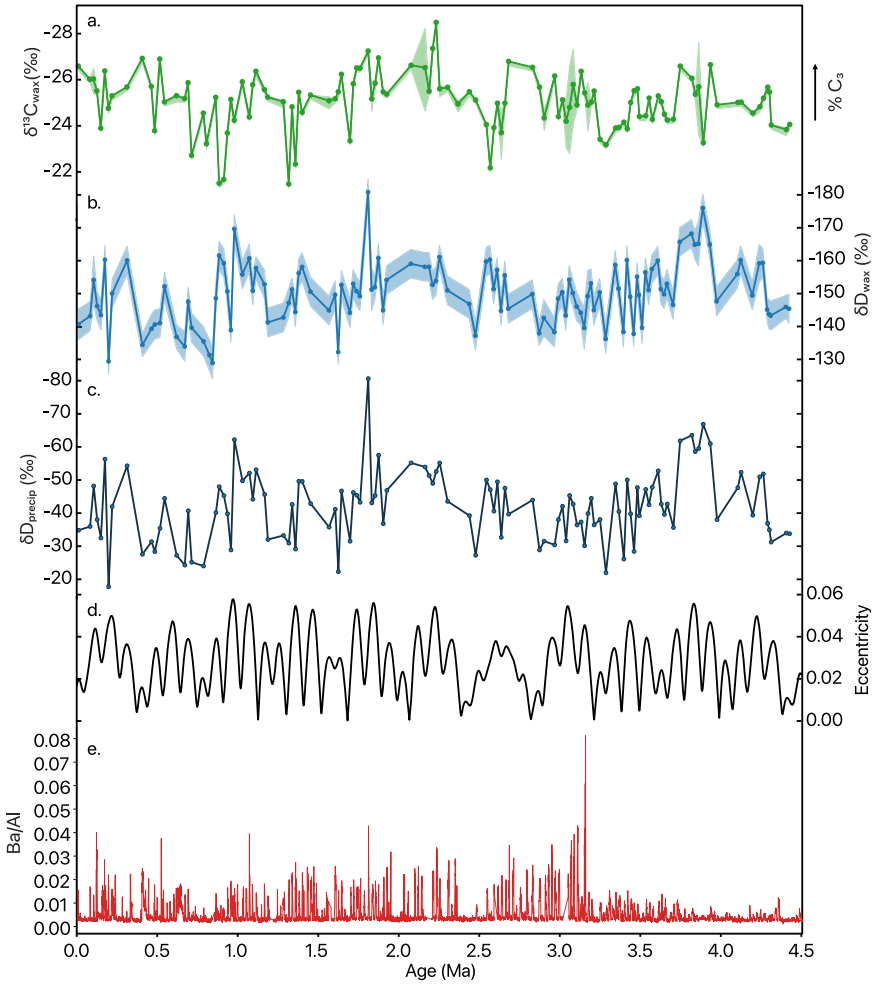

Fig. 2 Eastern Mediterranean leaf wax isotope records of hydroclimate and vegetation. Leaf wax isotope data generated for this study from ODP Sites 967 (post 3.2 Ma) and 966 (pre 3.0 Ma), including carbon isotopes with inferred %C_3 and 2 standard error mean (SEM) shaded (**a**), hydrogen isotopes 2 SEM shaded (**b**), δD of precipitation derived from the vegetation correction of δD_{wax} (**c**), the eccentricity of Earth's orbit[36] (**d**), and the ratio of Barium to Aluminum in the ODP Site 967 core to chemically denote the sapropel deposition[54] (**e**).

upon previous detailed absolute[48] and tuned[16,45] age models by refining the characterization of sapropel layers in the bottom sections of cores from Sites 967 Holes A and B and Site 966. We use the Laskar[36] orbital solution for up-to-date ages for insolation cycles. Thorough tuning via AnalySeries[49] of the density and reflectance parameters between the cores provides composite age and depth models going back 4.5 Myr (Fig. S1). All climate time series and subsequent interpretations are based off this ODP 966/967 composite record, hereafter ODP 966/967. The updated age model largely follows previous ones[16,45], with maximum changes on the order of 0.077 Myr compared with ref. [45] in the oldest interval of ODP Site 966.

Results

Leaf wax distributions and isotope values. The average chain length (ACL) of our samples is 27.2 and the average Carbon Preference Index (CPI), is 4.7 (minimum 1.7), similar to sedimentary samples with significant leaf wax *n*-acid contributions. There is no systematic trend in ACL or CPI, or other indicators such as largest compound or relative abundance of long:middle ($C_{26}+C_{28}+C_{30}+C_{32}$ / $C_{22}+C_{24}$) or long:short ($C_{26}+C_{28}+C_{30}+C_{32}$ / $C_{16}+C_{18}$) chain lengths, throughout the core. Thus, the long-chain *n*-acid distributions indicate a common leaf wax source and show no indication for the evolution of leaf wax molecular distributions since 4.5 Ma.

Leaf wax $\delta^{13}C$ values are significantly correlated between compound homologues ($r_{C26\text{-}C28}=0.73$, $p_{C26\text{-}C28}<0.0001$, $n=119$; $r_{C28\text{-}C30}=0.68$, $p_{C28\text{-}C30}<0.0001$, $n=121$). There are no systematic offsets in isotope value between the long chain compounds, although the amount of variance within C_{30} and C_{26} are higher than the C_{28} $\delta^{13}C_{wax}$ dataset. Following the correction for $\delta^{13}C_{CO2}$, the *n*-C_{28} $\delta^{13}C_{wax}$ reconstruction varies between −28.5‰ and −21.5‰, corresponding to 54% and 6% C_3 plant contributions, respectively, although with potentially large, propagated error bounds. The $\delta^{13}C_{wax}$ record does not contain a significant trend ($r=0.07$, $p>0.1$, $n=120$). $\delta^{13}C_{wax}$ is correlated to CPI ($r=-0.52$, $p<0.0001$, $n=145$), with more C_3-like values correlating to higher CPI values, but the isotope record is also correlated with various chain length indicators, such as ACL ($r=0.47$, $p<0.0001$, $n=145$) and long:short chain lengths ($r=0.41$, $p<0.0001$, $n=145$), indicating that longer compounds signify more grass-rich environments despite potential variations in the source of the waxes.

We observe significant correlations among δD_{wax} values of long-chain *n*-acids ($r_{C26\text{-}C28}=0.75$, $p_{C26\text{-}C28}<0.0001$, $n=120$; $r_{C28\text{-}C30}=0.63$, $p_{C28\text{-}C30}<0.0001$, $n=123$), suggesting leaf wax homologues in the samples are derived from a common vascular plant source. Similar to $\delta^{13}C_{wax}$, the structure of δD_{wax} between C_{26}, C_{28}, and C_{30} are very similar with no systematic offset. Thus, we use *n*-C_{28} to represent the long-chain δD_{wax}, which following

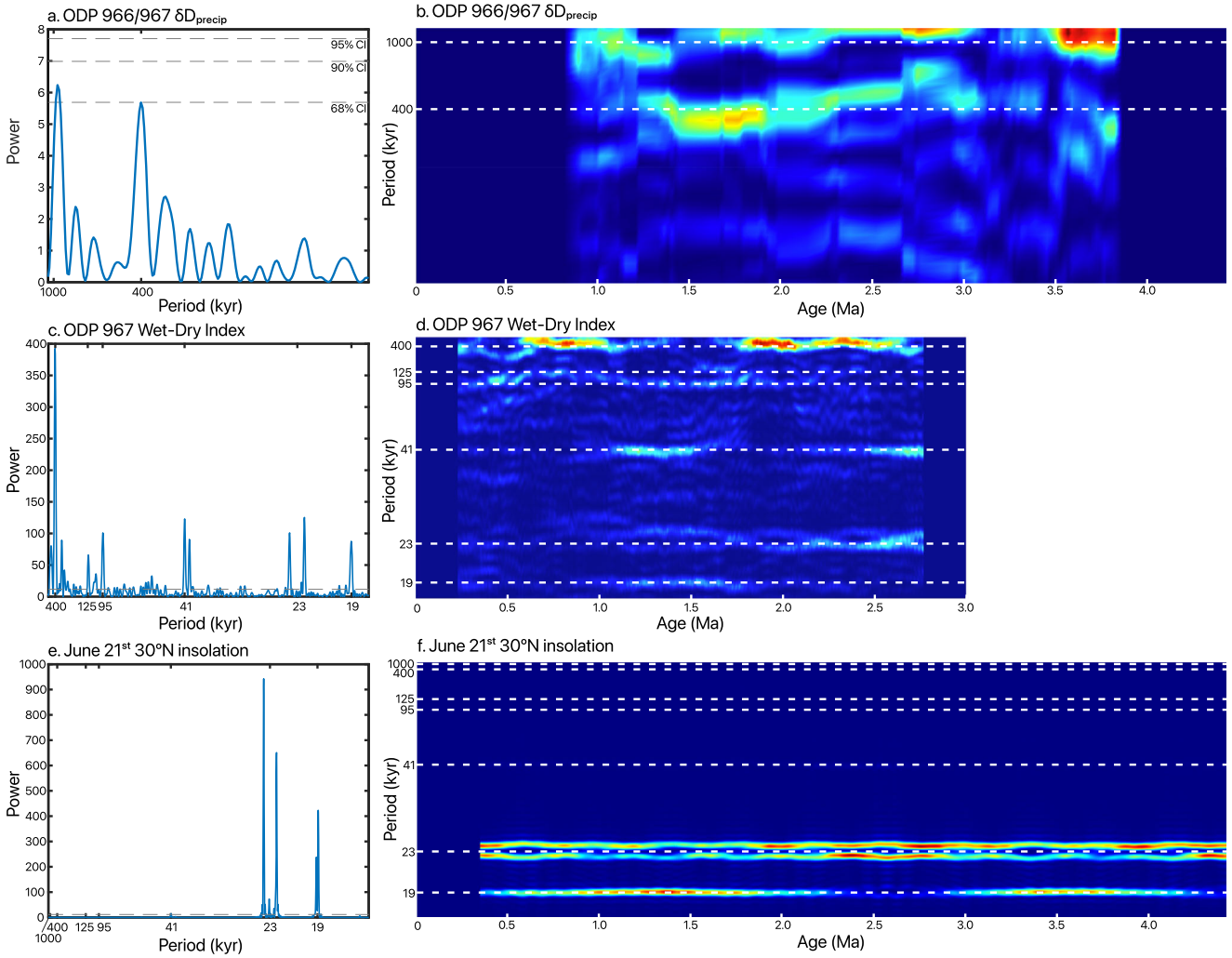

Fig. 3 Spectral analyses from leaf wax data, Wet-Dry Index, and insolation. Stationary and evolutive Lomb-Scargle spectral analyses of the δD_{precip} record from this study (**a**, **b**), the ref. [16] Wet-Dry Index (**c**, **d**), and mean insolation[36] on June 21st from 30°N (**e**, **f**). Confidence intervals (CI) of Lomb-Scargle spectral power denoted (left) in dashed gray lines.

the sea water δD correction has a mean of −150.1‰ and varies between −128.9‰ and −180.9‰ (Fig. 2b). The δD_{wax} record contains a weak, but significant, D-enrichment trend ($r = 0.22$, $p < 0.0001$, $n = 118$). δD_{wax} is not correlated with ACL ($r = -0.12$, $p > 0.1$, $n = 147$) nor CPI ($r = -0.10$, $p > 0.1$, $n = 147$), indicating the lack of influence that compound distribution has on the hydrogen isotope values. Using the $\delta^{13}C_{wax}$ for a vegetation correction of δD_{wax}, the δD_{precip} record has a mean of −41.9‰ and varies between −17.4‰ and −80.3‰ (Fig. 2c).

Spectral analysis of hydrologic timeseries. Both hydrogen and carbon leaf wax isotope datasets show ample variability throughout the last 4.5 Myr. Lomb-Scargle spectral analysis of the δD_{precip} record displays strong spectral power at the 400 kyr and 938 kyr bands (Fig. 3a). Considering the width of the low-frequency peak at half maximum (~860 kyr to 1.02 Myr; Fig. 3a), hereafter, we refer to this as a 1-Myr cycle. These strong periodicities are fairly consistent throughout the 4.5 Myr (with buffers of ~800 kyr on each end), yet the 1-Myr signal is more prominent before 2.7 Ma, and the 400-kyr signal is more prominent after 2.7 Ma (Fig. 3b). Gaussian 400-kyr- and 1-Myr-band-pass filters of δD_{precip} supports the spectral analysis results and are in phase with similarly filtered records of insolation (Fig. 4). When the dominant 400-kyr and 1-Myr cycles are removed from the δD_{precip} record, the residuals trend towards more D-enriched values with statistical significance ($r = -0.34$, $p < 0.001$, $n = 114$; Figs. 5a and 6a). The 400 kyr band comprises 10% of the variance of the δD_{precip} record, and the 1-Myr band comprises of 15%, with the residual representing 75% of the variance derived from non-orbital cycles.

Although we constrain the range of frequencies used as indicators of climate forcing (See Methods), a 2227 kyr cycle (close to the 2.3-Myr eccentricity cycle) appears to contribute to about a quarter of the total variance of the δD_{precip} record, reducing the contribution of non-orbital cycles to 50% (Fig. 6b). When all three of these cycles have been filtered out of the δD_{precip} record, there is no significant trend (Fig. 6b), implying that the low-frequency 2.3-Myr cycle may be the source of the enrichment trend over the last 4.5 Myr (Fig. 6a).

Similar techniques were applied to the Wet-Dry Index (Fig. 3c, d) and insolation (Fig. 3e, f), and spectral properties align with precession (19 and 23 kyr), obliquity (41 kyr), and eccentricity (95, 125, and 400 kyr). The 400-kyr band from the Wet-Dry Index appears significantly stronger than other cycles (Fig. 3c) and is consistently strong throughout the last 3 million years except between 1.7 and 1.0 Ma (Fig. 3d). Insolation documents precession-driven cycles at 19 and 23 kyr consistently dominating (Fig. 3e, f).

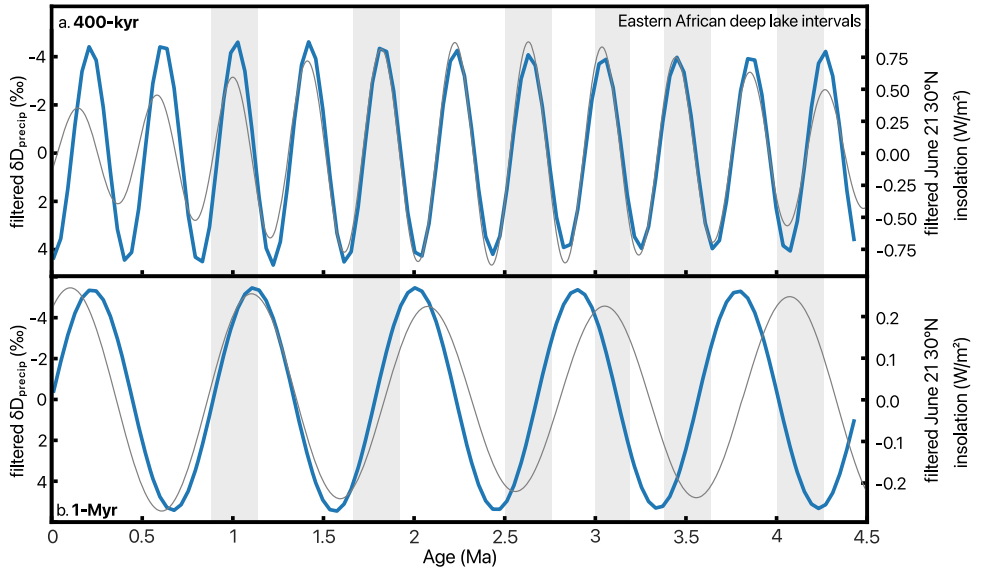

Fig. 4 Filtered leaf wax dataset compared with insolation and deep lake intervals. Gaussian filtering of δD_{precip} from this study (blue) and 30°N June 21st insolation (gray) at the 400-kyr (**a**) and 1-Myr (**b**) bands, with exact frequencies noted in Methods. Eastern African deep lake intervals from ref. [56] and ref. [35] highlighted in gray.

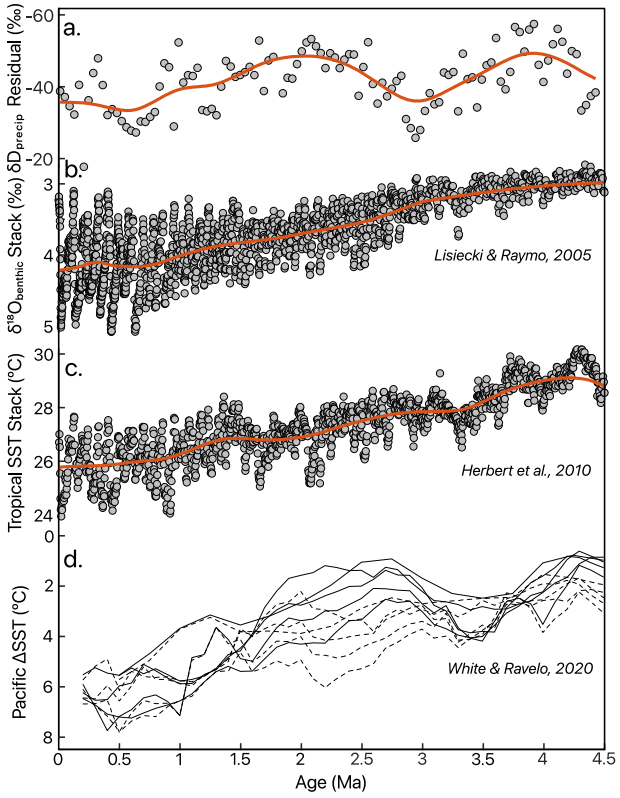

Fig. 5 Potential drivers of non-orbital trend and variability. The residual δD_{precip} variability from ODP 966/967 after removal of 400 kyr and 1 Myr cycles (**a**). This residual record is compared with potential external drivers including (**b**) the benthic stack[19], (**c**) the tropical sea surface temperature stack[66], and (**d**) Pacific SST gradient (west minus east) based off of Mg/Ca (solid lines) and $U^{K'}_{37}$ (dashed lines)[67]. 1-Myr moving average of records are documented in orange to demonstrate long-term trends and fluctuations.

Discussion

Cycles: the importance of low-frequency orbital periodicities. The presence and periodicity of sapropelic mud deposition exposed in Eastern Mediterranean outcrops and sediment cores highlights the importance of orbital cycles in the climate of the region. There is ample evidence for dominant precession control on monsoon intervals and sapropel occurrence, with some records also documenting obliquity and eccentricity signals. Reconstructions of hydroclimate[4,11–14,50] and lake level[34,51–53] in eastern Africa also document control by orbital precession and eccentricity. Modeling exercises further highlight the importance of orbital precession to the regional monsoon system in eastern Africa[2]. In theory, low-frequency orbital modulation of precession and obliquity signals should be apparent in long monsoon records. However, it has remained difficult to quantify the effects of low-frequency cycles due to the lack of long, well-dated records.

The δD_{precip} reconstructed here captures low frequency orbital cycles and their effect on monsoon strength during wet intervals. The dominant 400 kyr-band and 1 Myr-band cycles we find in northeast African precipitation (Fig. 3a) demonstrates that these low frequency cycles contribute significantly to modulation of the monsoon system. Spectral analysis demonstrates that these orbital cycles are robust in the δD_{precip} record and impact the magnitude of the wet endmembers found in the sapropel archives. Further, the specific timing and amplitude of these cycles in ODP 966/967 correspond extremely well with the same cycles observed in the low-latitude summer insolation timeseries (Fig. 4). The in-phase relationship of the δD_{precip} and insolation cycles suggests direct insolation forcing of the monsoon system through mechanisms that modify the strength of the largely precession-paced monsoon cycles. X-ray fluorescence (XRF) analyses and the associated ratios, such as Ti/Al, attributed to the relative proportions of aeolian (Ti) to riverine (Al) inputs[54,55], and indices, like the Wet-Dry Index from principal component analysis (PCA) in ref. [16], also demonstrate strong, persistent 400-kyr cyclicity (Fig. 3c), supporting the inference of monsoon precipitation variability at this timescale.

The strength and persistence of the 400-kyr eccentricity cycles in the climate record are notable because eccentricity has minimal influence over the absolute amount of insolation received on the Earth's surface, instead acting as an amplifier of the redistribution of energy by orbital precession (Fig. 3e). Through this

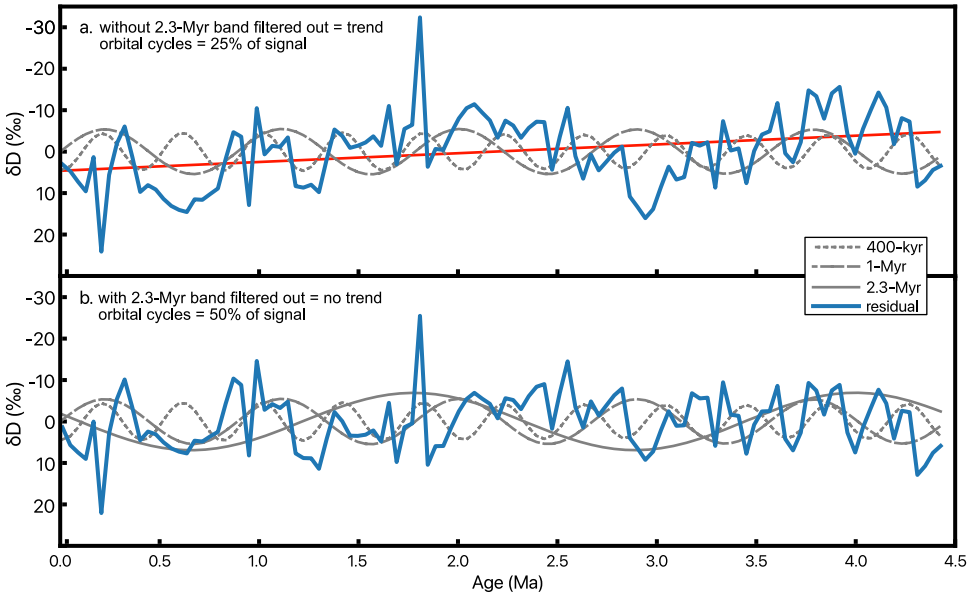

Fig. 6 Potential 2.3-Myr orbital cycle contribution to drying trend. The residual δD_{precip} variability from ODP 966/967 after removal of 400-kyr and 1-Myr periodicities (**a**) and 400-kyr, 1-Myr, and 2.3-Myr periodicities (**b**). This residual record exhibits a drying trend (red) when only the relatively higher frequencies are filtered out, but no trend when the 2.3-Myr cycle is also filtered out. The 2.3-Myr cycle contributes 25% of the original δD_{precip} reconstruction, bringing orbital influences up to 50% of the signal.

mechanism, 400-kyr modulation of precession maxima leads to the observed negative relationship of δD_{precip} of sapropel wet intervals with low-latitude summer insolation (Fig. 4a). More positive insolation maxima drive stronger monsoon rainfall leading to more negative δD_{precip} values. Supporting this interpretation, similarities between the timing of the 400-kyr wet intervals in the δD_{precip} record generally correspond to intervals of wide-spread deep lakes in eastern Africa[35,56] (Fig. 4). However, the continuous δD_{precip} record brings new detail to these long-term fluctuations and supports the idea that these lake basins likely experienced extreme dry intervals not fully represented in the geologic record. While the precession and 100-kyr eccentricity cycles have been linked with human evolutionary changes[8,12], there is a lack of statistical correlation between environmental variability in the 400-kyr cycle and speciation or extinction in Africa[15].

The 1-Myr cycle that also dominates the spectral power within ODP 966/967 δD_{precip} is potentially driven by low-frequency obliquity modulation with a 1.2 Myr periodicity, although this lies outside of the range of frequencies noted by spectral analysis. Obliquity and its modulation have a more direct influence on insolation at polar, rather than tropical latitudes. However, the 1.2 Myr cycle has been recorded in marine paleoclimate records that are of sufficient resolution and length[57], and other studies find 41-kyr-band obliquity cycle in the Mediterranean sapropel records[42,55], although it is relatively insignificant within the Wet-Dry Index[16] record (Fig. 3c, d). The presence of obliquity in low-latitude paleoclimate reconstructions, including δD_{precip} in this study, suggests that other orbital parameters, such as the cross-equatorial insolation gradient[58], could be important modulators of tropical precipitation strength, which may vary on an intracontinental scale. It is possible that the 1-Myr cycle is derived from currently unknown processes.

Through evolutive spectral analysis (Fig. 3b, d), we visualize how and when the strength of orbital cycles within the hydroclimate records increases and decreases through time. Within the δD_{precip} record from ODP 966/967, the 400 kyr and 1 Myr cycles are consistently strong since 4.5 Ma except when there is a shift from a strong 1 Myr cycle to a strong 400 kyr cycle around 2.7 Ma, and when the 400-kyr cycle weakens at 1 Ma (Fig. 3b). These shifts co-occur with major global boundary condition changes, namely the intensification of Northern Hemisphere glaciation in the late Pliocene and the mid-Pleistocene Transition. These changes to the global climate system have been shown to alter the significance and presence of eccentricity, obliquity, and precession in paleoclimate records[19,29,59]. However, the 400-kyr cycle of the Wet-Dry Index departs from this pattern, with a relative decrease in strength during 1.7–1.0 Ma (Fig. 3d).

Amplitudes: climate variability across orbital timescales. Previous work utilizing the sapropel deposition in the Mediterranean region has solidified the importance of precession on African climate[38]. Studies using the thickness of the dark sapropel layers have further advanced our understanding of the significant role that obliquity and eccentricity modulation may have on the EAM and WAM systems[60]. Analysis of geochemical proxies from the long, well-dated ODP 966/967 Eastern Mediterranean sediment cores have enabled us to resolve both high- and low-frequency climate fluctuations[55].

We applied stationary and evolutive spectral analysis to the Wet-Dry Index[16] to derive properties that indicate significant influences of precession, obliquity, and eccentricity modulation (Fig. 3c, d). While precession (19 kyr and 23 kyr), obliquity (41 kyr), and high-frequency eccentricity (95 kyr and 125 kyr) are significant in the Lomb-Scargle (Fig. 3c), both stationary and evolutive spectral analyses show that the eccentricity 400-kyr cycle is dominant over the last 3 Myr (Fig. 3c, d). This indicates an important role for the low frequency orbital cycles, supported by a recent compilation of African paleoclimate records[15]. However, a longer record is necessary to decipher even longer periodicities. Our new 4.5 Myr-long δD_{precip} record does not directly resolve precession or 41-kyr obliquity cycles, but we can examine how longer frequency orbital cycles might modulate monsoon strength. The strong 400-kyr eccentricity power in both the δD_{precip} and Wet-Dry Index records (Fig. 3a, c) highlights their similar forcing mechanism, despite the relatively weak spectral power found at this band in solar radiation (Fig. 3e). In

conjunction with the shorter, higher-resolution records, our longer, lower-resolution δD_{precip} record highlights the importance of the low frequency cycles, suggesting that a wide range of frequencies are critical, and potentially related, in tropical precipitation.

Rose et al.[14] presented high-resolution leaf wax isotopes from two 100-kyr-long intervals at 3.05 and 1.75 Ma also from ODP 966/967 (Fig. S2). They found ample precession-scale variability in each interval, with modulation of the variability driven strongly by eccentricity. Due to our sampling of sapropel intervals only, our new δD_{wax} data corresponds with the most depleted values in these high-resolution intervals (Fig. S2), often more negative compared with the precession-resolved data likely due to the targeted sapropel sampling and increased organic matter production during the wettest intervals. This illustrates how our sampling approach captures modulation of the D-depleted wet monsoon intervals, rather than the magnitude of individual precession-band monsoon cycles. The comparison reinforces how the amplitude of precession-scale climate variability can be assessed with our low-resolution sampling of the paleoclimate record.

The direct effects of high-frequency precession and obliquity seasonal insolation forcing on northern African monsoon strength have been well documented. Our record shows that low frequency orbital modulation of these cycles also affects monsoon strength, and that the scaling between low-frequency insolation forcing and monsoon strength has remained largely stationary over the past 4.5 Myr. The 400-kyr cycle likely reflects eccentricity modulation of maxima in precession-band insolation cycles and its effect on monsoon strength. In contrast, the 1-Myr cycles are potentially related to the 1.2-Myr modulation of obliquity and its effect on the cross-equatorial insolation gradient and moisture supply to the northern African monsoon system.

This long and astrochronologically dated record enables us to examine specific intervals with high- and low-amplitude climate variability. These high-amplitude precession-band packets of variability were particularly strong at 3.8, 1.8, 1.0, and 0.2 Ma according to the δD_{precip} reconstruction (Fig. 2c), times that have been highlighted in other studies as exhibiting evidence of deep lakes[56] (Fig. 4) and transitions in African climate variability[29]. These packets, which are likely to be common across northern and eastern Africa, have been linked to pulses in mammalian origination and extinction[61,62], although re-examination show only a single possible origination pulse at ~2.00–1.75 Ma[63]. These specific times are when both the 400-kyr and 1-Myr cycles contribute to more D-depleted values (Fig. 4), implying that the superposition of orbital drivers leads to major regional climate changes.

Trends: secular climate change over the Plio-Pleistocene. Sapropel records from the eastern Mediterranean clearly document orbitally driven oscillations, but long-term patterns have been historically difficult to quantify and disentangle from cyclicity with these methods. Trends are potentially more discernable using more quantitative measurements of hydroclimate, like from XRF analyses and associated ratios and indices[16]. However, other contributing factors, such as wind direction and basin integration area, could compound the long-term hydrological information. Eastern African records of Plio-Pleistocene climate using paleosol oxygen isotopes have supported long-term drying trends or shifts[25], but there is still ample disagreement in terms of the extent, timing, and drivers of aridification[64,65]. Further, low-frequency orbital cycles could potentially obscure these long-term signatures if the reconstruction is not of sufficient length.

In order to examine the non-orbital influences on the climate and environment over the Plio-Pleistocene, we remove the dominant 400-kyr and 1-Myr cycles from the leaf wax isotope record of precipitation to characterize residual fluctuations and identify non-orbital climate drivers over the Plio-Pleistocene, that make up 75% of the variance in the original δD_{precip} record (Fig. 5a). The derived residual δD_{precip} demonstrates clear long-term structure over the last 4.5 Myr with two wet-to-dry transitions occurring from ~4–3 Ma and ~2 Ma–present, with at least 20‰ variation (Fig. 5a). When viewed over the whole 4.5 Myr, precipitation strength appears to trend toward more arid conditions by ~10‰ (Fig. 5a), and there is a statistically significant trend (Fig. 6a).

Disentangling the potential drivers of secular change is furthered by comparison of the residual δD_{precip} record with published records of global ice volume[19], tropical sea surface temperature[66] (SST), and Pacific SST gradients[67] (Fig. 5). All of these records demonstrate a long-term trend in aridification, increasing ice volume and global cooling, tropical SST cooling, and increasing Pacific SST gradients, respectively. These processes are likely related, as global sea level[68] and SST cooling could lead to aridification in eastern Africa[1,69,70] and the zonal SST gradient in the Pacific has been linked with terrestrial precipitation in Africa[23]. For instance, paleoclimate reconstruction studies ascribe the anomalously low SST gradient in the late Pliocene to global warmth and more El Niño-like conditions[67,71,72]. Characterization of Indian Ocean zonal SST gradients throughout the Plio-Pleistocene will improve the interpretations of the residual precipitation mechanisms, but the Pacific gradient throughout this time shares a similar structure, with a shallow gradient during wet northeast African interval and a gradual steepening trend during the drying starting at the beginning of the Pleistocene[67] (Fig. 5d). Our data suggests that just before 3 Ma may have been anomalously dry in the context of a wetter Pliocene (Fig. 5a), which could potentially be driven by the tropical SST gradient shifts, although they show a maximum a few hundred thousand years earlier (Fig. 5d). Terrestrial hydroclimate in the tropical mid-Pliocene has also been shown to be driven by vegetative greening[69], yet $\delta^{13}C_{wax}$ (Fig. 2a) shows no trend throughout the duration of our Plio-Pleistocene study interval, suggesting that far-afield processes, like Indian and Atlantic Ocean SST and their effects on moisture supply and convective processes over eastern Africa, drive the long-term aridification in northeast Africa.

However, it is also possible that this structure in the residual record is oscillatory, and thus driven by a longer orbital periodicity, such as the 2.3 Myr eccentricity cycle. We additionally filter out the 2.3 Myr cycle to examine this possibility (Fig. 6b). When the 2.3 Myr power of our δD_{precip} is quantified, it contributes nearly 25% of the entire structure of the original precipitation reconstruction. Thus, if this is a real signature, despite not being a robust measure due to the length of the δD_{precip} record, the non-orbital contributions to δD_{precip} variance are reduced from 75% (Fig. 6a) to 50% (Fig. 6b). Regardless, ample (at least 50%) hydroclimate change is derived from non-orbital sources, which likely drive trends in the mean climate, rather than modulation of a precession signal, as our targeted sampling allows us to characterize.

Hominin evolution and environmental change. The strong, consistent 400-kyr band detected in the new δD_{precip} record and previously published Wet-Dry Index[16] is attributed to eccentricity forcing, which modulates precession-band variability and, therefore, contributes to the amplitude of environmental change. Indeed, in comparison with a higher-resolution record of leaf wax

isotopes across multiple organic-rich and organic-poor layers[14], we do find that our sapropel dataset tracks the wet endmembers of a highly-variable, precession-driven reconstruction (Fig. S2). Further, the sapropel intervals provide additional information on long term variability characteristics when compared with the eastern African soil carbonate records ($\delta^{18}O_{sc}$ and $\delta^{13}C_{sc}$), which typically form in dry seasons and/or hot conditions. The $\delta^{18}O_{sc}$ and $\delta^{13}C_{sc}$ records reveal gradual aridification and C_4 expansion, respectively, throughout the Plio-Pleistocene in eastern Africa, at least since 2 Ma[25]. Other offshore $\delta^{13}C_{wax}$ records indicate long term fluctuations in northeast African environments in the Pliocene[73]. The stable mean of ODP 966/967 $\delta^{13}C_{wax}$ along with the enrichment trend in $\delta^{13}C_{sc}$ may indicate that vegetation variability increased through time, which is consistent with well-resolved records of vegetation from eastern Africa[10,74]. While ODP 966/967 δD_{precip} and $\delta^{18}O_{sc}$ both trend towards more arid conditions, the increase in carbon isotope-derived environmental fluctuation may have had a significant effect on hominin evolution by selecting for more generalist traits and potentially hosting more dramatic shifts between drastically different ecosystems[7].

The northeast African region is central to the story of hominin evolution, particularly in terms of dispersal routes of the genus *Homo*. The northeastern Sahara is a hypothesized dispersal route along fluvial or coastal corridors (e.g., the Nile River Valley and the Red Sea), and climate[6] and agent-based modeling[75] has shown that aridity and open vegetation in the region limit these pathways. It is likely that stronger, expanded, and more northward EAM and eastward WAM precipitation would bring respite and resources for hominins in northeast Africa. The expansion of C_3 plants (i.e., trees and shrubs in this region), as seen in ^{13}C-depleted intervals (Fig. 2a), likely enhanced the connectivity of potential habitats, which has been suggested to be a main factor in dispersal characteristics[76]. We find that there were many periods of more woody Green Sahara intervals, including a particularly woody vegetation (over 50% C_3) interval at ~2.2 Ma in the Nile River catchment (Fig. 2a), generally coinciding with the first dispersal out of Africa[77,78]. A large, vegetated area connecting east and northern Africa may have triggered a pull-type response in hominins that were now able to survive using larger cranial capacity[79] and move in the lush, ecologically connected, region of northeastern Africa.

Some of the particularly woody intervals (^{13}C-depleted) coincide with relatively arid times, potentially limiting the likelihood of human migration due to lack of water resources and indicating that each Green Sahara interval may not have had ideal conditions for hominin habitat expansion. Similarly, the coincidence of the grassiest (^{13}C-enriched) intervals with moderate or extreme wetness, as documented by δD_{precip}, could indicate that additional WAM moisture into to the leaf wax catchment area of northeast Africa during precession minima led to a more vegetated northeast Sahara relative to the typical desert environment. Thus, in some of the Green Sahara intervals, C_4 grassland expansion may have created linked corridors through which hominins could have dispersed.

Conclusions

Through the generation of long, well-dated, quantitative records of both precipitation and vegetation of northern Africa, we discern long-term trends and a large range of spectral properties in the climate and environment of northeast Africa over the Plio-Pleistocene. We find a mixture of signals from insolation-driven monsoon oscillations and secular variations likely caused by some combination of globally driven ice, temperature, and atmospheric dynamics. Low-frequency orbital cycles, driven by both obliquity and eccentricity, are prominent in northeast African precipitation, despite the minimal direct influence from low-latitude summer insolation. When these low-frequency cycles are removed from the original precipitation record, we find that at least 50% of variability is caused by non-orbital influences.

Environmental change between C_3- and C_4-dominated ecosystems in northeastern Africa would have impacted hominin resource base and dispersal pathways. Connectivity of habitable zones and resource abundance, conditions more likely during eccentricity-modulated humid, C_3-rich environments, serving as potential migration pathways, could have favored dispersals around and out of Africa at critical time intervals, particularly at 2.2 Ma, when the environment was the most C_3-plant-dominated in the entire study interval. The northeast African region acted as a connecting pathway out of and into Africa, and ideal climatological and environmental conditions were needed in this area to serve as a reliable habitat for early humans.

Climate and ecosystem fluctuations were large on orbital timescales throughout the Plio-Pleistocene, and likely prior to the period of study, suggesting that there were numerous Green Sahara intervals going back millions of years[80]. These likely occurred nearly every ~21 kyr cycle and would have been particularly strong during high eccentricity intervals on 100 kyr and 400 kyr cycles. Our record also suggests that monsoonal variability is potentially modulated by the 1.2-Myr obliquity cycle and the 2.3-Myr eccentricity cycle. These findings, along with prior documentation of these low-frequency cycles, indicate complex mixtures of orbital forcings across latitudes as well as secular trends and variations. Orbital-scale variability was larger than any long-term trends or shifts, and thus had a larger influence on environmental sensitivity, but the increase in the number of reconstructions that can resolve cycles, amplitudes, and trends of African paleoclimate are central to the robust testing of hominin evolutionary hypotheses.

Methods

Organic geochemical and isotopic analyses. The sampling approach exclusively targets sapropel layers in order to develop a long record of orbital and secular trends of wet Mediterranean intervals. This strategy allowed analysis of trends in the full 4.5 Myr record while greatly reducing the number of samples that would be required to resolve precession and longer orbital variations. Each sample comprises the entire thickness of a sapropel layer in the core, which ranged from 2 to 22 cm. The whole sapropel layer was sampled to avoid aliasing, and instead to characterize the amplitude of the wet signal above the threshold needed for sapropel generation, deposition, and preservation. Thus, sediment samples may integrate varying amounts of time, but provide information on the average amplitude of the wet end member. However, due to necessary levels of organic content for leaf wax isotope quantification, ghost sapropels and oxidated sections of sapropels were not sampled, and thus bias may have been introduced to favor wet and dry periods, depending on the extent of oxidation[45]. Further, ref. [14] (Fig. S2) discovered very low organic matter concentrations in the nannofossil ooze layers between sapropels, meaning integrated samples are strongly biased to the high organic content at the peak sapropel level.

Organic geochemical analysis was performed on 156 samples and resulted in isotope data from 123 sapropels that cover most of the humid intervals from 4.5 Ma to present. Seven sediment samples did not contain sufficient organic material for robust isotope measurements; 20 samples were analyzed from the same sapropel layer in different sediment cores and were averaged for the final datasets used for interpretations; and six samples were from parts of a single sapropel that was deposited across core section breaks and were weight averaged. New isotope analyses

were combined with 24 previously measured data initially presented in ref. [81].

Lipids from freeze-dried sediment were extracted with dichloromethane:methanol (DCM:MeOH; 9:1 v/v) using a DIONEX Accelerated Solvent Extractor 350. The lipids were split into neutral, acid, and polar fractions over an aminopropyl silica gel column with DCM:*iso*-propanol (2:1 v/v), diethyl ether:acetic acid (24:1 v/v), and methanol as eluents, respectively. The acid fractions were methylated with acidified methanol at 60 °C overnight to produce fatty acid methyl esters (FAMEs). FAMEs were then separated from hydroxy FAMEs with a silica gel column eluted with hexane, DCM (FAME), and MeOH (OH-FAME). A sodium phthalate standard with a previously determined non-exchangeable hydrogen and carbon isotope composition was methylated along with samples to determine the isotope composition of the C and H added during methylation.

From the post-methylation DCM fraction, FAME concentrations were measured using an Agilent GC-MSD/FID (Agilent 7890a GC and 5975 C MSD) equipped with a DB-5ms column (30 m × 0.25 mm × 0.25 µm). Distributions were summarized using the average Chain length[82] (ACL) and tested for degradation using the Carbon Preference Index[83] (CPI), which, when used for *n*-alkanoic acids, quantifies the even-over-odd chain length preference to estimate degradation of the waxes, as has been done in previous studies involving leaf wax FAMEs[12]. Both ACL and CPI are calculated using the peak areas of even and odd chain lengths from C_{22} to C_{32}.

Hydrogen carbon isotopes of waxes (δD_{wax} and $\delta^{13}C_{wax}$) were analyzed on a Thermo Delta V Plus isotope ratio mass spectrometer (IRMS) coupled to an Isolink with a Thermo Trace GC Ultra and are reported on the VSMOW and VPBD scales, respectively (Fig. 2). Samples were measured in triplicate for δD_{wax} and duplicate for $\delta^{13}C_{wax}$, and δD_{wax} measurements were corrected for the isotopic composition of the added methyl group during methylation using the phthalic acid methyl ester standard. The H_3^+ factor was quantified daily[84,85]. An 'in-house' standard was used to monitor instrument performance. Standard mixtures of *n*-alkanes with known isotope values (Mix A7 from the Schimmelmann Laboratory at Indiana University) were injected periodically for isotopic calibration. Standard error means calculated using the protocol from ref. [86] were 0.09‰ for $\delta^{13}C_{wax}$ and 4.30‰ for δD_{wax}. These uncertainties incorporate both the analytical uncertainty on the FAME and Mix A7 measurements, and the uncertainty in realizing the VPDB and VSMOW scales.

Framework for interpreting leaf wax isotopes. Leaf wax biomarkers are a novel paleoclimate proxy that are preserved in a range of archives and amenable to compound specific isotope analyses in order to reconstruct the climate and environmental conditions of terrestrial plants. Plants produce epicuticular waxes to shield leaf surfaces from evaporation and physical damage[87]. These waxes may be ablated and transported by aeolian and fluvial processes to lakes and oceans, where they accumulate and are preserved in sediment over geological time. The waxes include long-chain *n*-alkanoic acids, which we use to reconstruct water isotope compositions.

Leaf wax δD is primarily controlled by δD_{precip}[88,89], which, in tropical Africa, is dominantly driven by regional atmospheric dynamics that govern rainfall amount[90,91]. A variety of observational[91,92], modeling[93], and paleoclimate[4,12,14,58,70,94] studies have revealed δD_{precip} to be highly sensitive to changes in eastern and western African rainfall on orbital timescales. δD_{precip} can be influenced by a variety of other processes such as moisture source and transport, and a variety of convective processes including the location of convective cells[95]. Therefore, we interpret δD_{precip} as a qualitative indicator of rainfall amount, consistent with previous studies in the region[4,11,12,14,17,95].

Plants utilize several distinct photosynthetic pathways to fix carbon dioxide[96], and these pathways result in unique carbon isotopic fractionation patterns reflected in $\delta^{13}C$ of plant tissues including leaf waxes. This allows for the identification of C_3 versus C_4 plant types from sedimentary $\delta^{13}C_{wax}$, which is reflected in surface ocean sediments along the African margin[97]. In eastern Africa, C_3 plants are dominantly woody dicots (trees and shrubs), whereas C_4 plants are dominantly grasses and some sedges[98,99]. The relative abundance of trees and grasses is strongly influenced by precipitation, due to a variety of physiological differences related to water stress, although vegetation can also be influenced by rainfall seasonality, growing season temperature, pCO_2, herbivory, and fire[26,100–104]. $\delta^{13}C_{wax}$ records from paleolake sediment have documented that eastern African vegetation fluctuates throughout the entire C_3-C_4 spectrum on orbital timescales[12,17,102,105,106].

Corrections for changes in the isotopic compositions in the source water and atmospheric CO_2 are applied to the δD_{wax} and $\delta^{13}C_{wax}$ measurements, respectively. We use a benthic foraminifera $\delta^{18}O$ stack[20] to estimate past ocean water isotopes to correct the δD_{wax} for ice volume effects on δD (Fig. S3). We normalize the $\delta^{18}O_{benthic}$ at each insolation cycle to modern, extract the ice volume component using the $\delta^{18}O_{benthic}$ at the Last Glacial Maximum, and convert it to δD based on the slope and intercept relationship between seawater and the global meteoric water line (Equation S1; Fig. S3). We then apply this anomaly to each study interval to obtain an ice volume-corrected signal of δD_{wax}. Using a 3 Myr-moving average of $\delta^{13}C_{CO2}$ from ref. [107], we correct our $\delta^{13}C_{wax}$ measurements for changes in the isotopic makeup of atmospheric CO_2 by interpolating the ages to those of our samples.

C_3 and C_4 plants fractionate hydrogen to different degrees during leaf wax synthesis due to differing metabolic pathways and plant physiologies. This causes different apparent fractionations between leaf waxes and precipitation ($\varepsilon_{wax\text{-}P}$), which can affect paleoclimate records based on δD_{wax} if vegetation changes[89]. We calculated a 'landscape fractionation'[108] based upon C_3-C_4 plant proportions to calculate δD_{precip} values from δD_{wax}. To calculate $\%C_3$ vegetation on the landscape, we develop a linear mixing model using $\delta^{13}C_{CO2}$-corrected[109,110] $\delta^{13}C_{wax}$ endmember values for C_3 and C_4 plant types[111], calculated as −35.4‰ for the C_3 *n*-C_{28} acid endmember and −20.5‰ for the C_4 endmember, after ref. [14]. After applying this C_3-C_4 mixing model to our $\delta^{13}C_{wax}$ data, we then applied $\varepsilon_{wax\text{-}P}$ values of −94‰ and −122‰ for C_3 and C_4 vegetation, respectively[89], to correct for 'vegetation effects' on δD_{wax} and estimate δD_{precip}[112], which will be used for further time series analyses of hydroclimate change.

Time series analyses. We employ a suite of time series analyses to better understand the drivers of climate and environmental change over the last 4.5 Myr in the Northeast African region. We calculated the Pearson correlation coefficient between various climate and orbital parameters in the ODP 966/967 record. Lomb-Scargle spectral analysis of nonuniformly sampled data with the *plomb* function in the MATLAB Signal Processing Toolbox[113] was performed to elucidate cycles of significant spectral density (Fig. 3). We focus on the band frequencies between 50% of the Nyquist frequency (25% of the mean sampling frequency) and 25% of the total length of the record. Evolutive Lomb-Scargle spectral analysis was also performed on the δD_{precip} record, the Wet-Dry Index[16], and mean June 21st insolation at 30°N[36] using a moving (1 data point step) window

size of 32 data-points (~566 kyr) for δD_{precip}, 856 data-points (~428 kyr) for the Wet-Dry Index, and 714 data-points (714 kyr) for insolation (Fig. 3).

Remaining time series analytical techniques required linearly interpolated data to achieve evenly sampled records. Filtering exercises were performed on the newly generated δD_{precip} record and mean June 21st insolation at 30°N[36] using QAnalySeries[114] to isolate (band-pass) periodicities associated with eccentricity (400 kyr and 2.3 Myr) and obliquity (1.2 Myr) (Fig. 4). The specific frequencies and widths used for filtering were targeted using the Lomb-Scargle spectral analysis results of δD_{precip} (2.49743 ± 0.2, 1.06632 ± 0.15, 0.448977 ± 0.14) and insolation (2.475 ± 0.2; 1 ± 0.2; 0.45 ± 0.175). These significant spectra within the pre-determined frequency bounds in the ODP 966/967 reconstructions were then subtracted from the original δD_{precip} record to yield a δD_{precip} residual dataset, which had one outlier removed, that captures the non-orbital evolution of δD (Fig. 5a). Further, the 2.3 Myr cycle was also filtered out of δD_{precip} to compare the relative influence of secular trends and low frequency cycles (Fig. 6). By dividing the variance of each filtered band by the variance of the original δD_{precip} record, we then determined the percent contributions of the orbitally driven cycles and the secular residual variability to the measured paleoclimate record.

Data availability

Leaf wax isotope data from ODP 160 Sites 966 and 967 generated in this study, along with composite depth scales for both sites in Supplementary Table 1, are available at the NOAA NCEI World Data Service for Paleoclimatology at https://www.ncei.noaa.gov/access/paleo-search/study/38561. Wet-Dry Index data from ODP 160 Site 967 are available through Grant et al.[16], https://doi.org/10.1016/j.quascirev.2017.07.005.

Received: 27 April 2023; Accepted: 29 September 2023;
Published online: 09 October 2023

References

1. Otto-Bliesner, B. L. et al. Coherent changes of southeastern equatorial and northern African rainfall during the last deglaciation. *Science* **346**, 1223–1227 (2014).
2. Kutzbach, J. E. et al. African climate response to orbital and glacial forcing in 140,000-y simulation with implications for early modern human environments. *Proc. Natl Acad. Sci.* **117**, 2255–2264 (2020).
3. Chandan, D. & Peltier, W. R. African humid period precipitation sustained by Robust vegetation, soil, and lake feedbacks. *Geophys. Res. Lett.* **47**, 1–12 (2020).
4. Tierney, J. E., DeMenocal, P. B. & Zander, P. D. A climatic context for the out-of-Africa migration. *Geology* **45**, 1023–1026 (2017).
5. Schaebitz, F. et al. Hydroclimate changes in eastern Africa over the past 200,000 years may have influenced early human dispersal. *Commun. Earth Environ.* **2**, 123 (2021).
6. Timmermann, A. et al. Climate effects on archaic human habitats and species successions. *Nature* https://doi.org/10.1038/s41586-022-04600-9 (2022).
7. Potts, R. Evolution and climate variability. *Science* **273**, 992 (1996).
8. Potts, R. & Faith, J. T. Alternating high and low climate variability: the context of natural selection and speciation in Plio-Pleistocene hominin evolution. *J. Human Evol.* **87**, 5–20 (2015).
9. Castañeda, I. S. et al. Wet phases in the Sahara/Sahel region and human migration patterns in North Africa. *Proc. Natl Acad. Sci.* **106**, 20159–20163 (2009).
10. Lupien, R. L. et al. Eastern African environmental variation and its role in the evolution and cultural change of Homo over the last 1 million years. *J. Human Evol.* **157C**, 103028 (2021).
11. Lupien, R. L. et al. Orbital controls on eastern African hydroclimate in the Pleistocene. *Sci. Rep.* **12**, 3170 (2022).
12. Lupien, R. L. et al. A leaf wax biomarker record of early Pleistocene hydroclimate from West Turkana, Kenya. *Quat. Sci. Rev.* **186**, 225–235 (2018).
13. Joordens, J. C. A. et al. An astronomically-tuned climate framework for hominins in the Turkana Basin. *Earth Planet. Sci. Lett.* **307**, 1–8 (2011).
14. Rose, C., Polissar, P. J., Tierney, J. E., Filley, T. & deMenocal, P. B. Changes in northeast African hydrology and vegetation associated with Pliocene–Pleistocene sapropel cycles. *Philos. Trans. R. Soc. Lond. B Biol. Sci.* **371**, 20150243 (2016).
15. Cohen, A. S. et al. Plio-Pleistocene environmental variability in Africa and its implications for mammalian evolution. *Proc. Natl Acad. Sci.* https://doi.org/10.1073/pnas.2107393119 (2022).
16. Grant, K. M. et al. A 3 million year index for North African humidity/aridity and the implication of potential pan-African Humid periods. *Quat. Sci. Rev.* **171**, 100–118 (2017).
17. Lupien, R. L. et al. Vegetation change in the Baringo Basin, East Africa across the onset of Northern Hemisphere glaciation 3.3–2.6 Ma. *Palaeogeogr. Palaeoclimatol. Palaeoecol.* **570**, 109426 (2021).
18. Yost, C. L. et al. Phytoliths, pollen, and microcharcoal from the Baringo Basin, Kenya reveal savanna dynamics during the Plio-Pleistocene transition. *Palaeogeogr. Palaeoclimatol. Palaeoecol.* **570**, 109779 (2021).
19. Lisiecki, L. E. & Raymo, M. E. A Pliocene-Pleistocene stack of 57 globally distributed benthic δ18O records. *Paleoceanography* **20**, PA1003 (2005).
20. Westerhold, T. et al. An astronomically dated record of Earth's climate and its predictability over the last 66 million years. *Science* **369**, 1383–1387 (2020).
21. Zachos, J. C., Shackleton, N. J., Revenaugh, J. S., Pälike, H. & Flower, B. P. Climate response to orbital forcing across the Oligocene-miocene boundary. *Science* **292**, 274–278 (2001).
22. Raymo, M. E. The initiation of Northern Hemisphere glaciation. *Ann. Rev. Earth Planet. Sci.* **22**, 353–383 (1994).
23. Brierley, C. M. & Fedorov, A. V. Relative importance of meridional and zonal sea surface temperature gradients for the onset of the ice ages and Pliocene-Pleistocene climate evolution. *Paleoceanography* **25**, PA2214 (2010).
24. Ravelo, A. C., Andreasen, D. H., Lyle, M., Lyle, A. O. & Wara, M. W. Regional climate shifts caused by gradual global cooling in the Pliocene epoch. *Nature* **429**, 263–267 (2004).
25. Levin, N. E. Environment and climate of early human evolution. *Ann. Rev. Earth Planet. Sci.* **43**, 405–429 (2015).
26. Dupont, L. M., Caley, T. & Castañeda, I. S. Effects of atmospheric CO2 variability of the past 800kyr on the biomes of southeast Africa. *Clim. Past* **15**, 1083–1097 (2019).
27. Feakins, S. J., deMenocal, P. B. & Eglinton, T. I. Biomarker records of late Neogene changes in northeast African vegetation. *Geology* **33**, 977–980 (2005).
28. Polissar, P. J., Rose, C., Uno, K. T., Phelps, S. R. & deMenocal, P. B. Synchronous rise of African C4 ecosystems 10 million years ago in the absence of aridification. *Nat. Geosci.* **12**, 657–660 (2019).
29. deMenocal, P. B. Plio-Pleistocene African climate. *Science* **270**, 53–59 (1995).
30. deMenocal, P. B. African climate change and faunal evolution during the Pliocene–Pleistocene. *Earth Planet. Sci. Lett.* **220**, 3–24 (2004).
31. Larrasoaña, J. C., Roberts, A. P., Rohling, E. J., Winklhofer, M. & Wehausen, R. Three million years of monsoon variability over the northern Sahara. *Clim. Dyn.* **21**, 689–698 (2003).
32. Larrasoaña, J. C., Roberts, A. P. & Rohling, E. J. Magnetic susceptibility of eastern Mediterranean marine sediments as a proxy for Saharan dust supply? *Marine Geol.* **254**, 224–229 (2008).
33. Skonieczny, C. et al. Monsoon-driven Saharan dust variability over the past 240,000 years. *Sci. Adv.* **5**, eaav1887 (2019).
34. Trauth, M. H., Larrasoaña, J. C. & Mudelsee, M. Trends, rhythms and events in Plio-Pleistocene African climate. *Quat. Sci. Rev.* **28**, 399–411 (2009).
35. Trauth, M. H., Maslin, M. A., Deino, A. & Strecker, M. R. Late Cenozoic moisture history of East Africa. *Science* **309**, 2051–2053 (2005).
36. Laskar, J. et al. A long-term numerical solution for the insolation quantities of the Earth. *Astronomy Astrophys.* **428**, 261–285 (2004).
37. Rossignol-Strick, M., Nesteroff, W., Olive, P. & Vergnaud-Grazzini, C. After the deluge: Mediterranean stagnation and sapropel formation. *Nature* **295**, 105 (1982).
38. Rossignol-Strick, M. Mediterranean Quaternary sapropels, an immediate response of the African monsoon to variation of insolation. *Palaeogeogr. Palaeoclimatol. Palaeoecol.* **49**, 237–263 (1985).
39. Larrasoaña, J. C. A review of West African monsoon penetration during Green Sahara periods; implications for human evolution and dispersals over the last three million years. *Oxford Open Clim. Change* **1**, kgab011 (2021).
40. Rohling, E. J., Marino, G. & Grant, K. M. Mediterranean climate and oceanography, and the periodic development of anoxic events (sapropels). *Earth Sci. Rev.* **143**, 62–97 (2015).
41. Hilgen, F. J. Astronomical calibration of Gauss to Matuyama sapropels in the Mediterranean and implication for the geomagnetic polarity time scale. *Earth Planet. Sci. Lett.* **104**, 226–244 (1991).
42. Lourens, L. J., Hilgen, F. J., Raffi, I. & Vergnaud-Grazzini, C. Early Pleistocene chronology of the vrica section (Calabria, Italy). *Paleoceanography* **11**, 797–812 (1996).
43. Lourens, L. J. et al. Evaluation of the Plio-Pleistocene astronomical timescale. *Paleoceanography* **11**, 391–413 (1996).
44. Rossignol-Strick, M. African monsoons, an immediate climate response to orbital insolation. *Nature* **304**, 46–49 (1983).

107. Tipple, B. J., Meyers, S. R. & Pagani, M. Carbon isotope ratio of Cenozoic CO_2: a comparative evaluation of available geochemical proxies. *Paleoceanography* **25**, PA3202 (2010).
108. Magill, C. R., Ashley, G. M. & Freeman, K. H. Water, plants, and early human habitats in eastern Africa. *Proc. Natl Acad. Sci.* **110**, 1175–1180 (2013).
109. Francey, R. J. et al. A 1000-year high precision record of δ13C in atmospheric CO_2. *Tellus B* **51**, 170–193 (1999).
110. Keeling, C. D. et al. Atmospheric CO_2 and $13CO_2$ Exchange with the Terrestrial Biosphere and Oceans from 1978 to 2000: Observations and Carbon Cycle Implications. in *A History of Atmospheric CO_2 and Its Effects on Plants, Animals, and Ecosystems* (eds. Baldwin, I. T. et al.) 83–113 (Springer, 2005). https://doi.org/10.1007/0-387-27048-5_5.
111. Chikaraishi, Y., Naraoka, H. & Poulson, S. R. Hydrogen and carbon isotopic fractionations of lipid biosynthesis among terrestrial (C3, C4 and CAM) and aquatic plants. *Phytochemistry* **65**, 1369–1381 (2004).
112. Clark, I. & Fritz, P. *Environmental Isotopes in Hydrogeology*. (CRC Press, 2013). https://doi.org/10.1201/9781482242911.
113. MathWorks. *MATLAB Signal Processing Toolbox: User's Guide*. (The MathWorks, 2022).
114. Kotov, S. & Pälike, H. QAnalySeries—a cross-platform time series tuning and analysis tool. *ESS Open Archive* (2018).

Acknowledgements

We wish to thank Wei Huang and Helen Habicht for laboratory management, and two anonymous reviewers for improving our manuscript. This research used samples and data provided by the International Ocean Discovery Program (IODP). This research was generously supported by the Center for Climate and Life at Columbia University. We would like to thank two anonymous reviewers for their helpful suggestions and comments.

Author contributions

R.L. conducted data analysis, data interpretation, supervision, and led manuscript preparation. K.U. conducted data interpretation, supervision, and edited the manuscript. C.R. conducted sediment sampling and laboratory analyses, and edited the manuscript. C.H. conducted data analysis and data interpretation. N.dR. conducted laboratory analyses. P.d.M. conducted funding acquisition, data interpretation, and edited the manuscript. P.P. conceptualized the study, conducted data interpretation, supervision, and edited the manuscript.

Competing interests

The authors declare no competing interests.

Additional information

Supplementary information The online version contains supplementary material available at https://doi.org/10.1038/s43247-023-01034-7.

Correspondence and requests for materials should be addressed to Rachel Lupien.

Peer review information *Communications Earth and Environment* thanks the anonymous reviewers for their contribution to the peer review of this work. Primary Handling Editors: Yama Dixit and Aliénor Lavergne. A peer review file is available.

Reprints and permission information is available at http://www.nature.com/reprints

Publisher's note Springer Nature remains neutral with regard to jurisdictional claims in published maps and institutional affiliations.

Plio-Pleistocene climate and environmental cycles, amplitudes, and trends of northeast Africa

Supplementary Information

Rachel Lupien[1,2,3], Kevin Uno[3,2], Cassaundra Rose[4], Nicole deRoberts[2], Cole Hazan[2], Peter de Menocal[5], Pratigya Polissar[6]

[1]Aarhus University, Department of Geoscience, Aarhus, Denmark
[2]Columbia University, Lamont-Doherty Earth Observatory, Palisades, USA
[3]Harvard University, Department of Human Evolutionary Biology, Cambridge, USA
[4]United States Climate Alliance, Augusta, USA
[5]Woods Hole Oceanographic Institution, Woods Hole, USA
[6]University of California, Santa Cruz, Department of Ocean Sciences, Santa Cruz, USA

Contents of this file

Additional Supporting Information

Supplementary Notes 1*: Composite Depth and Age Model*

1.1. Composite depth model

We used the following techniques to obtain a composite depth model to enable the future placement of any sample from ODP Leg 160 on a common depth and age model. Using AnalySeries[1] age model and time series analysis program, we created tie lines and interpolations between them using visual analysis of common maxima and minima within core property datasets from ODP 160[2].

First, we compared reflectance data from site 967 to correlate holes B and C to A to bring site 967 to a common depth scale. Next, we correlated reflectance data from 966B also to 967A to get both cores on a common depth scale. Due to the lack of reflectance data in some of the other 966 holes, we tuned magnetic susceptibility from site 966 holes A, C, and D, to 966B, which has already been tuned to 967A. Therefore, we have converted meters below seafloor (mbsf) of all holes from sites 966 and 967 to a common depth scale (mcd), which is equivalent to mbsf from 967A. All conversions are available for future use in Supplemental Table 1.

As mentioned in the main text, some samples appear to be taken from the same sapropel, yet we obtained isotope measurements from each individually. Thus, with new mcd values for each sample, we weight-averaged the samples taken from a sapropel that spans a core boundary (i.e., the sapropel spanned 5 cm of drive 2 and 10 cm of drive 3, so the isotope measurement from the sample in drive 3 makes up 2/3 of the final value). For samples from the same sapropel that appears in two or more different sites or holes, these were simply averaged.

1.2. Age Model

Each sapropel sample with new composite depth value was assigned an insolation cycle (icycle) using previous designations from Emeis et al.[3] and Grant et al.[4]. Four samples appeared to be off of an insolation maximum due to their depth assignments and were excluded from the final δD_{precip} record used for time series analysis. The bottom three samples of 966 were re-assigned specific numbered insolation cycles (icycles) due to new composite depth calculations and the assumption of a relatively linear sedimentation rate. The age of these icycles were then assigned using the more up-to-date astronomical solution from Laskar et al.[5]. No 3-kyr lag was applied, as earlier sapropel studies suggested[3], due to the argument by Grant et al. (2017) that this phase lag has not been tested in sapropel intervals prior to the most recent glacial cycle. With new composite depths for all holes at sites 966 and 967, and updated age assignments for each sapropel, we present a new age model (Fig. S1) based on years of prior work with relative linearity apart from an anomaly around 2 Ma.

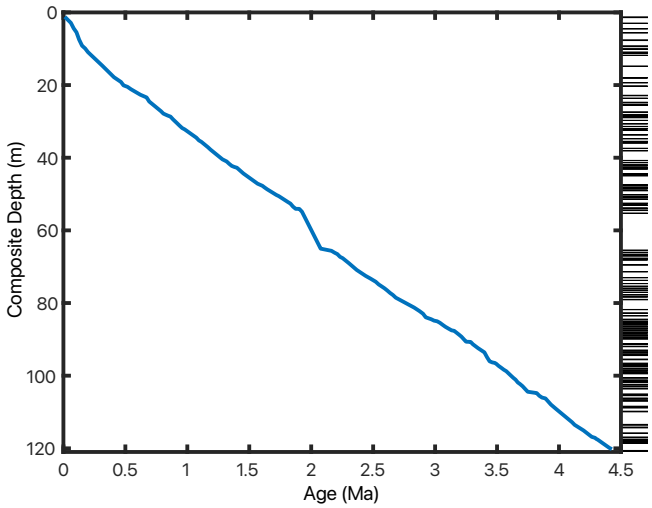

Figure S1. Composite age-depth model for ODP Leg 160 Sites 966 and 967. Sapropel layers used for age model development plotted on the right.

Supplementary Notes 2: *δD_{precip} across sampling scales*

We compare our new δD_{wax} from the same ODP160 Site 967 as Rose et al.[6] who measured δD_{wax} in two high-resolution time windows, before and after the onset of

Northern Hemisphere Glaciation. As our sampling method was to sample the integrated sapropel layers, we expect that our isotopic values would be more depleted than records across strata, like in Rose et al.[6].

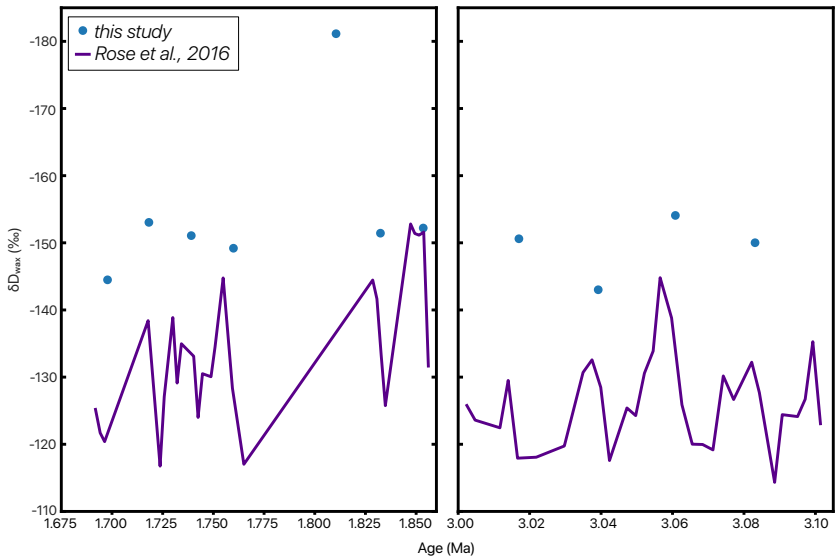

Figure S2. Relatively high-resolution δD_{wax} from Rose et al.[6] in purple with new relatively low-resolution δD_{wax} from this study in blue. Our eccentricity-paced wet endmember samples track the D-depleted amplitude changes in the previous reconstruction.

2. Sea water isotope correction

Because sea water isotopes varied in the past due to changes in temperature and ice volume, a correction to the measured δD_{wax} has been applied, based on Rose et al. (2016). We use a benthic foraminifera $\delta^{18}O$ stack[7] to estimate past ocean water isotopes to correct the δD_{wax} for different source water δD (Figure S3). We first normalize the stack to the modern $\delta^{18}O_{benthic}$ value (3.52‰), and subsequently extract the ice volume component of the stack by normalizing the glacial-interglacial variability by dividing by the normalized Last Glacial Maximum value (1.833‰). Finally, we convert the $\delta^{18}O_{IV}$ to δD_{IV} based on the 8:1 slope and intercept relationship between seawater and the global meteoric water line (Equation S1; Figure S3). We then use delta equation [8] to apply this ice volume correction to each study interval of δD_{wax}.

$$\delta D_{IV} = [(\delta^{18}O_{benthic} - \delta^{18}O_{modern})/(\delta^{18}O_{LGM} - \delta^{18}O_{modern})] \times 8 \quad \text{(S1)}$$

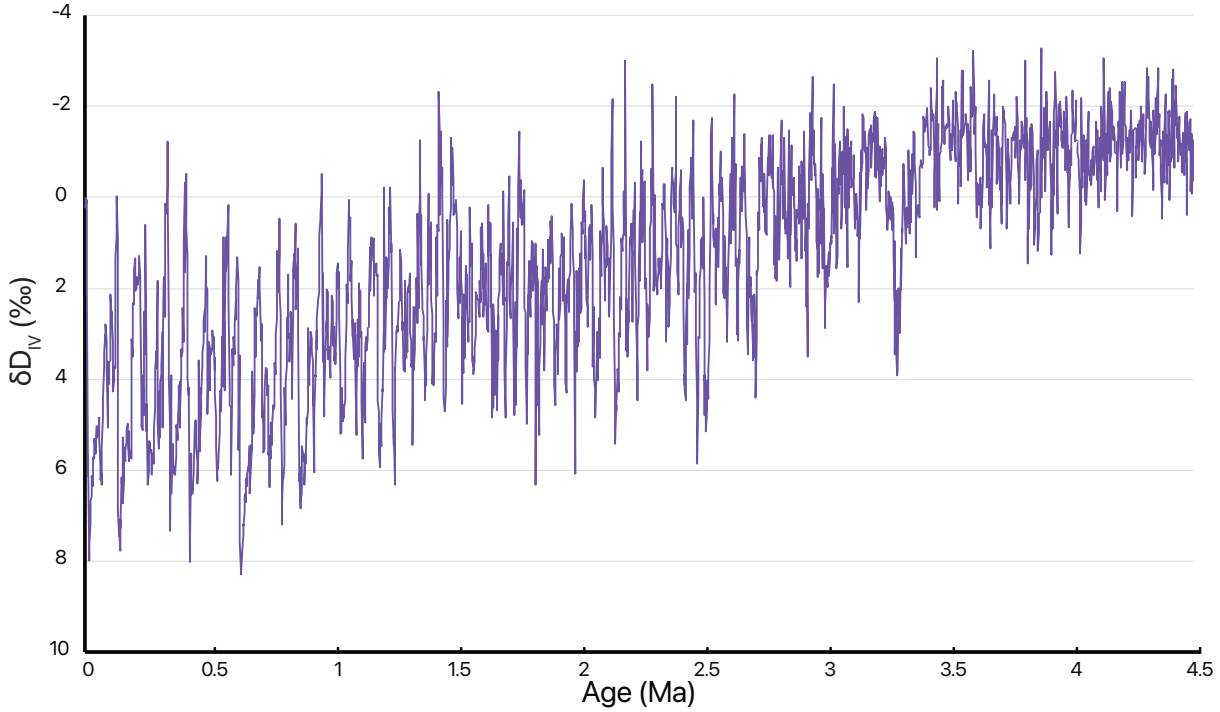

Figure S3. Calculated δD of the ice volume component of benthic foraminiferal isotope variance for use of ice volume corrections of systems in δD space.

Supplementary References

1. Paillard, D., Labeyrie, L. & Yiou, P. AnalySeries 2.0: Macintosh program performs time-series analsyis. *Eos Transactions American Geophysical Union* (1996).
2. Emeis, K.-C., Robertson, A. H. F. & Richter, C. Shipboard Scientific Party ODP Leg 160. in *Proceeding of the Ocean Drilling Program, Scientific Results* vol. 160 972 (1996).
3. Emeis, K.-C., Sakamoto, T., Wehausen, R. & Brumsack, H.-J. The sapropel record of the eastern Mediterranean Sea—results of Ocean Drilling Program Leg 160. *Palaeogeogr. Palaeoclimatol. Palaeoecol.* **158**, 371–395 (2000).
4. Grant, K. M. *et al.* A 3 million year index for North African humidity/aridity and the implication of potential pan-African Humid periods. *Quat. Sci. Rev.* **171**, 100–118 (2017).
5. Laskar, J. *et al.* A long-term numerical solution for the insolation quantities of the Earth. *Astron. Astrophys.* **428**, 261–285 (2004).
6. Rose, C., Polissar, P. J., Tierney, J. E., Filley, T. & deMenocal, P. B. Changes in northeast African hydrology and vegetation associated with Pliocene–Pleistocene sapropel cycles. *Philos. Trans. R. Soc. Lond. B Biol. Sci.* **371**, (2016).
7. Westerhold, T. *et al.* An astronomically dated record of Earth's climate and its predictability over the last 66 million years. *Science* **369**, 1383–1387 (2020).
8. Clark, I. & Fritz, P. *Environmental Isotopes in Hydrogeology*. (CRC Press, 2013). doi:10.1201/9781482242911.

45. Emeis, K.-C., Sakamoto, T., Wehausen, R. & Brumsack, H.-J. The sapropel record of the eastern Mediterranean Sea—results of Ocean Drilling Program Leg 160. *Palaeogeogr. Palaeoclimatol. Palaeoecol.* **158**, 371–395 (2000).
46. Dinerstein, E. et al. An ecoregion-based approach to protecting half the terrestrial realm. *BioScience* **67**, 534–545 (2017).
47. Emeis, K.-C., Robertson, A. H. F. & Richter, C. Shipboard scientific party ODP Leg 160. *Proc. Ocean Drill. Progr. Sci. Results* **160**, 972 (1996). in.
48. Sakamoto, T., Janecek, T. & Emeis, K.-C. Continuous sedimentary sequences from the eastern Mediterranean Sea: composite depth sections. in *Proceedings of the Ocean Drilling Program. Scientific results* Vol. 160 37–59 (Ocean Drilling Program, 1998).
49. Paillard, D., Labeyrie, L. D. & Yiou, P. AnalySeries 1.0: a Macintosh software for the analysis of geophysical time-series. *Eos* **77**, 379 (1996).
50. Tierney, J. E. et al. Northern hemisphere controls on tropical southeast African climate during the past 60,000 years. *Science* **322**, 252–255 (2008).
51. Kingston, J. D., Deino, A. L., Edgar, R. K. & Hill, A. Astronomically forced climate change in the Kenyan Rift Valley 2.7–2.55 Ma: implications for the evolution of early hominin ecosystems. *J. Hum. Evol.* **53**, 487–503 (2007).
52. Nutz, A., Schuster, M., Boës, X. & Rubino, J.-L. Orbitally-driven evolution of Lake Turkana (Turkana Depression, Kenya, EARS) between 1.95 and 1.72 Ma: a sequence stratigraphy perspective. *J. Afr. Earth Sci.* **125**, 230–243 (2017).
53. Westover, K. S. et al. Diatom paleolimnology of late Pliocene Baringo Basin (Kenya) paleolakes. *Palaeogeogr. Palaeoclimatol. Palaeoecol.* **570**, 109382 (2021).
54. Grant, K. M. et al. Organic carbon burial in Mediterranean sapropels intensified during Green Sahara Periods since 3.2 Myr ago. *Commun. Earth Environ.* **3**, 11 (2022).
55. Hennekam, R. et al. Accurately calibrated X-ray fluorescence core scanning (XRF-CS) record of Ti / Al reveals Early Pleistocene aridity and humidity variability over North Africa and its close relationship to low-latitude insolation. *Clim. Past* **18**, 2509–2521 (2022).
56. Maslin, M. A. et al. East African climate pulses and early human evolution. *Quat. Sci. Rev.* **101**, 1–17 (2014).
57. Holbourn, A., Kuhnt, W., Schulz, M., Flores, J.-A. & Andersen, N. Orbitally-paced climate evolution during the middle Miocene "Monterey" carbon-isotope excursion. *Earth Planet. Sci. Lett.* **261**, 534–550 (2007).
58. O'Mara, N. A. et al. Pleistocene drivers of Northwest African hydroclimate and vegetation. *Nat. Commun.* **13**, 3552 (2022).
59. Hays, J. D., Imbrie, J. & Shackleton, N. J. Variations in the Earth's orbit: pacemaker of the ice ages. *Science* **194**, 1121–1132 (1976).
60. Bosmans, J. H. C., Hilgen, F. J., Tuenter, E. & Lourens, L. J. Obliquity forcing of low-latitude climate. *Clim. Past* **11**, 1335–1346 (2015).
61. Vrba, E. S. Turnover-pulses, the Red Queen, and related topics. *Am. J. Sci.* **293**, 418–452 (1993).
62. Vrba, E.S. On the connections between paleoclimate and evolution. In: Vrba, E.S., Denton, G.H., Partridge, T.C., Burckle, L.H. (Eds.). *Paleoclimate and Evolution, with Emphasis on Human Origins,* 24–45 (Yale University Press, 1995).
63. Bibi, F. & Kiessling, W. Continuous evolutionary change in Plio-Pleistocene mammals of eastern Africa. *Proceedings of the National Academy of Sciences* **112**, 10623–10628 (2015).
64. Blumenthal, S. A. *et al.* Aridity and hominin environments. *Proceedings of the National Academy of Sciences***114**, 7331–7336 (2017).
65. Trauth, M. H. et al. Northern Hemisphere Glaciation, African climate and human evolution. *Quat. Sci. Rev.* **268**, 107095 (2021).
66. Herbert, T. D., Peterson, L. C., Lawrence, K. T. & Liu, Z. Tropical ocean temperatures over the past 3.5 million years. *Science* **328**, 1530–1534 (2010).
67. White, S. M. & Ravelo, A. C. The Benthic B/Ca Record at Site 806: New Constraints on the Temperature of the West Pacific Warm Pool and the "El Padre" State in the Pliocene. *Paleoceanogr. Paleoclimatol.* **35**, e2019PA003812 (2020).
68. Windler, G., Tierney, J. E. & deMenocal, P. B. Hydroclimate variability in the equatorial Western Indian Ocean for the last 250,000 years. *Paleoceanogr. Paleoclimatol.* **38**, e2022PA004530 (2023).
69. Feng, R. et al. Past terrestrial hydroclimate sensitivity controlled by Earth system feedbacks. *Nat. Commun.* **13**, 1306 (2022).
70. Tierney, J. E. & deMenocal, P. B. Abrupt shifts in Horn of Africa hydroclimate since the Last Glacial Maximum. *Science* **342**, 843–846 (2013).
71. Fedorov, A. V., Burls, N. J., Lawrence, K. T. & Peterson, L. C. Tightly linked zonal and meridional sea surface temperature gradients over the past five million years. *Nat. Geosci.* **8**, 975–980 (2015).
72. Wara, M. W., Ravelo, A. C. & Delaney, M. L. Permanent El Niño-like conditions during the Pliocene warm period. *Science* **309**, 758–761 (2005).
73. Liddy, H. M., Feakins, S. J. & Tierney, J. E. Cooling and drying in northeast Africa across the Pliocene. *Earth Planet. Sci. Lett.* **449**, 430–438 (2016).
74. Potts, R. et al. Increased ecological resource variability during a critical transition in hominin evolution. *Sci. Adv.* **6**, 1–15 (2020).
75. Timbrell, L., Grove, M., Manica, A., Rucina, S. & Blinkhorn, J. A spatiotemporally explicit paleoenvironmental framework for the Middle Stone Age of eastern Africa. *Sci. Rep.* **12**, 3689 (2022).
76. Scerri, E. M. L. et al. Did our species evolve in subdivided populations across Africa, and why does it matter? *Trends Ecol. Evol.* **33**, 582–594 (2018).
77. Ferring, R. et al. Earliest human occupations at Dmanisi (Georgian Caucasus) dated to 1.85–1.78 Ma. *Proc. Natl Acad. Sci.* **108**, 10432–10436 (2011).
78. Zhu, Z. et al. Hominin occupation of the Chinese Loess Plateau since about 2.1 million years ago. *Nature* **559**, 608–612 (2018).
79. Shultz, S. & Maslin, M. A. Early human speciation, brain expansion and dispersal influenced by African climate pulses. *PloS One* **8**, e76750 (2013).
80. Larrasoaña, J. C., Roberts, A. P. & Rohling, E. J. Dynamics of green Sahara periods and their role in hominin evolution. *PloS One* **8**, e76514 (2013).
81. Rose, C. *Late Cenozoic Evolution of Aridity and C4 Vegetation in North Africa.* Vol. PhD (Columbia University, 2015).
82. Castañeda, I. S. et al. Middle to Late Pleistocene vegetation and climate change in subtropical southern East Africa. *Earth Planet. Sci. Lett.* **450**, 306–316 (2016).
83. Bray, E. E. & Evans, E. D. Distribution of n-paraffins as a clue to recognition of source beds. *Geochim. Cosmochim. Acta* **22**, 2–15 (1961).
84. Sessions, A. L., Burgoyne, T. W. & Hayes, J. M. Determination of the H3 factor in hydrogen isotope ratio monitoring mass spectrometry. *Anal. Chem.* **73**, 200–207 (2001).
85. Sessions, A. L., Burgoyne, T. W. & Hayes, J. M. Correction of H3+ contributions in hydrogen isotope ratio monitoring mass spectrometry. *Anal. Chem.* **73**, 192–199 (2001).
86. Polissar, P. J. & D'Andrea, W. J. Uncertainty in paleohydrologic reconstructions from molecular δD values. *Geochim. Cosmochim. Acta* **129**, 146–156 (2014).
87. Eglinton, G. & Hamilton, R. J. Leaf epicuticular waxes. *Science* **156**, 1322–1335 (1967).
88. Garcin, Y. et al. Hydrogen isotope ratios of lacustrine sedimentary n-alkanes as proxies of tropical African hydrology: insights from a calibration transect across Cameroon. *Geochim. Cosmochim. Acta* **79**, 106–126 (2012).
89. Sachse, D. et al. Molecular paleohydrology: interpreting the hydrogen-isotopic composition of lipid biomarkers from photosynthesizing organisms. *Ann. Rev. Earth Planet. Sci.* **40**, 221–249 (2012).
90. Dansgaard, W. Stable isotopes in precipitation. *Tellus* **16**, 436–468 (1964).
91. Rozanski, K., Araguás-Araguás, L. & Gonfiantini, R. Isotopic patterns in modern global precipitation. in *Climate change in Continental Isotopic Records,* eds. Swart, P. K., Lohmann, K. C., McKenzie, J. & Savin, S. **78** (1993).
92. Vuille, M., Werner, M., Bradley, R. S., Chan, R. Y. & Keimig, F. Stable isotopes in East African precipitation record Indian Ocean zonal mode. *Geophys. Res. Lett.* **32**, L21705 (2005).
93. Risi, C., Bony, S. & Vimeux, F. Influence of convective processes on the isotopic composition (δ18O and δD) of precipitation and water vapor in the tropics: 2. Physical interpretation of the amount effect. *J. Geophys. Res. Atmos.* **113**, 1–12 (2008).
94. Tierney, J. E., Russell, J. M., Damsté, J. S. S., Huang, Y. & Verschuren, D. Late Quaternary behavior of the East African monsoon and the importance of the Congo Air Boundary. *Quat. Sci. Rev.* **30**, 798–807 (2011).
95. Costa, K., Russell, J. M., Konecky, B. L. & Lamb, H. F. Isotopic reconstruction of the African humid period and Congo air boundary migration at Lake Tana, Ethiopia. *Quat. Sci. Rev.* **83**, 58–67 (2014).
96. O'Leary, M. H. Carbon isotope fractionation in plants. *Phytochemistry* **20**, 553–567 (1981).
97. Collins, J. A. et al. Interhemispheric symmetry of the tropical African rainbelt over the past 23,000 years. *Nat. Geosci.* **4**, 42–45 (2011).
98. Cerling, T. E. & Harris, J. M. Carbon isotope fractionation between diet and bioapatite in ungulate mammals and implications for ecological and paleoecological studies. *Oecologia* **120**, 347–363 (1999).
99. Tieszen, L. L., Senyimba, M. M., Imbamba, S. K. & Troughton, J. H. The distribution of C3 and C4 grasses and carbon isotope discrimination along an altitudinal and moisture gradient in Kenya. *Oecologia* **37**, 337–350 (1979).
100. Asner, G. P. et al. Large-scale impacts of herbivores on the structural diversity of african savannas. *Proc. Natl Acad. Sci. USA* **106**, 4947–4952 (2009).
101. Bond, W. J. What limits trees in C4 grasslands and savannas? *Ann. Rev. Ecol. Evol. Syst.* **39**, 641–659 (2008).
102. Ivory, S. J., Lézine, A., Vincens, A. & Cohen, A. S. Waxing and waning of forests: late Quaternary biogeography of southeast Africa. *Glob. Change Biol.* **24**, 2939–2951 (2018).
103. Lehmann, C. E. R. et al. Savanna vegetation-fire-climate relationships differ among continents. *Science* **343**, 548–552 (2014).
104. Sankaran, M. et al. Determinants of woody cover in African savannas. *Nature* **438**, 846–849 (2005).
105. Colcord, D. E. et al. Sub-Milankovitch paleoclimatic and paleoenvironmental variability in East Africa recorded by Pleistocene lacustrine sediments from Olduvai Gorge, Tanzania. *Palaeogeogr. Palaeoclimatol. Palaeoecol.* **495**, 284–291 (2018).
106. Magill, C. R., Ashley, G. M. & Freeman, K. H. Ecosystem variability and early human habitats in eastern Africa. *Proc. Natl Acad. Sci.* **110**, 1167–1174 (2013).

Plio-Pleistocene climate and environmental cycles, amplitudes, and trends of northeast Africa

Supplementary Information

Rachel Lupien[1,2,3], Kevin Uno[3,2], Cassaundra Rose[4], Nicole deRoberts[2], Cole Hazan[2], Peter de Menocal[5], Pratigya Polissar[6]

[1]Aarhus University, Department of Geoscience, Aarhus, Denmark
[2]Columbia University, Lamont-Doherty Earth Observatory, Palisades, USA
[3]Harvard University, Department of Human Evolutionary Biology, Cambridge, USA
[4]United States Climate Alliance, Augusta, USA
[5]Woods Hole Oceanographic Institution, Woods Hole, USA
[6]University of California, Santa Cruz, Department of Ocean Sciences, Santa Cruz, USA

Contents of this file

Additional Supporting Information

Supplementary Notes 1*: Composite Depth and Age Model*

1.1. Composite depth model

We used the following techniques to obtain a composite depth model to enable the future placement of any sample from ODP Leg 160 on a common depth and age model. Using AnalySeries[1] age model and time series analysis program, we created tie lines and interpolations between them using visual analysis of common maxima and minima within core property datasets from ODP 160[2].

First, we compared reflectance data from site 967 to correlate holes B and C to A to bring site 967 to a common depth scale. Next, we correlated reflectance data from 966B also to 967A to get both cores on a common depth scale. Due to the lack of reflectance data in some of the other 966 holes, we tuned magnetic susceptibility from site 966 holes A, C, and D, to 966B, which has already been tuned to 967A. Therefore, we have converted meters below seafloor (mbsf) of all holes from sites 966 and 967 to a common depth scale (mcd), which is equivalent to mbsf from 967A. All conversions are available for future use in Supplemental Table 1.

As mentioned in the main text, some samples appear to be taken from the same sapropel, yet we obtained isotope measurements from each individually. Thus, with new mcd values for each sample, we weight-averaged the samples taken from a sapropel that spans a core boundary (i.e., the sapropel spanned 5 cm of drive 2 and 10 cm of drive 3, so the isotope measurement from the sample in drive 3 makes up 2/3 of the final value). For samples from the same sapropel that appears in two or more different sites or holes, these were simply averaged.

1.2. Age Model

Each sapropel sample with new composite depth value was assigned an insolation cycle (icycle) using previous designations from Emeis et al.[3] and Grant et al.[4]. Four samples appeared to be off of an insolation maximum due to their depth assignments and were excluded from the final δD_{precip} record used for time series analysis. The bottom three samples of 966 were re-assigned specific numbered insolation cycles (icycles) due to new composite depth calculations and the assumption of a relatively linear sedimentation rate. The age of these icycles were then assigned using the more up-to-date astronomical solution from Laskar et al.[5]. No 3-kyr lag was applied, as earlier sapropel studies suggested[3], due to the argument by Grant et al. (2017) that this phase lag has not been tested in sapropel intervals prior to the most recent glacial cycle. With new composite depths for all holes at sites 966 and 967, and updated age assignments for each sapropel, we present a new age model (Fig. S1) based on years of prior work with relative linearity apart from an anomaly around 2 Ma.

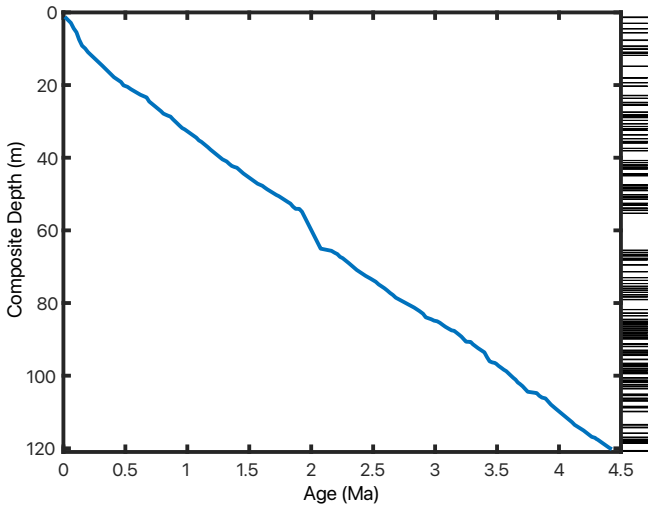

Figure S1. Composite age-depth model for ODP Leg 160 Sites 966 and 967. Sapropel layers used for age model development plotted on the right.

Supplementary Notes 2: *δD_{precip} across sampling scales*

We compare our new δD_{wax} from the same ODP160 Site 967 as Rose et al.[6] who measured δD_{wax} in two high-resolution time windows, before and after the onset of

Northern Hemisphere Glaciation. As our sampling method was to sample the integrated sapropel layers, we expect that our isotopic values would be more depleted than records across strata, like in Rose et al.[6].

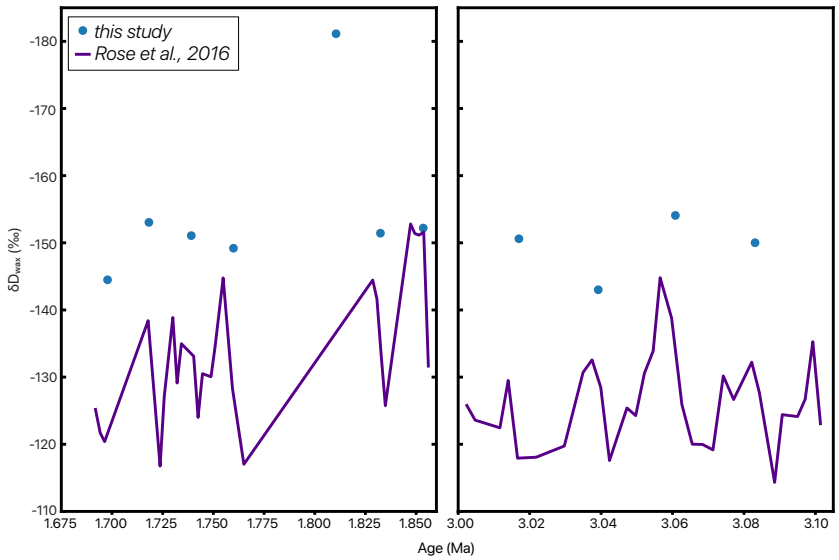

Figure S2. Relatively high-resolution δD_{wax} from Rose et al.[6] in purple with new relatively low-resolution δD_{wax} from this study in blue. Our eccentricity-paced wet endmember samples track the D-depleted amplitude changes in the previous reconstruction.

2. Sea water isotope correction

Because sea water isotopes varied in the past due to changes in temperature and ice volume, a correction to the measured δD_{wax} has been applied, based on Rose et al. (2016). We use a benthic foraminifera $\delta^{18}O$ stack[7] to estimate past ocean water isotopes to correct the δD_{wax} for different source water δD (Figure S3). We first normalize the stack to the modern $\delta^{18}O_{benthic}$ value (3.52‰), and subsequently extract the ice volume component of the stack by normalizing the glacial-interglacial variability by dividing by the normalized Last Glacial Maximum value (1.833‰). Finally, we convert the $\delta^{18}O_{IV}$ to δD_{IV} based on the 8:1 slope and intercept relationship between seawater and the global meteoric water line (Equation S1; Figure S3). We then use delta equation [8] to apply this ice volume correction to each study interval of δD_{wax}.

$$\delta D_{IV} = [(\delta^{18}O_{benthic} - \delta^{18}O_{modern})/(\delta^{18}O_{LGM} - \delta^{18}O_{modern})] \times 8 \quad \text{(S1)}$$

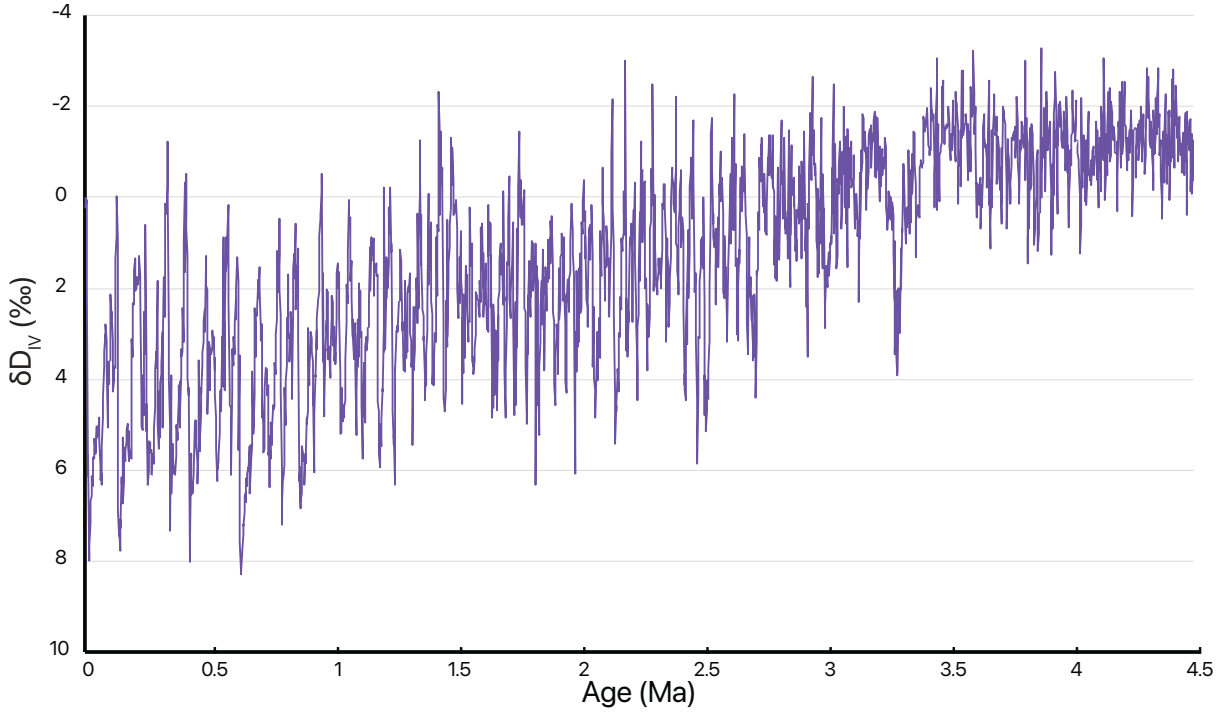

Figure S3. Calculated δD of the ice volume component of benthic foraminiferal isotope variance for use of ice volume corrections of systems in δD space.

Supplementary References

1. Paillard, D., Labeyrie, L. & Yiou, P. AnalySeries 2.0: Macintosh program performs time-series analsyis. *Eos Transactions American Geophysical Union* (1996).
2. Emeis, K.-C., Robertson, A. H. F. & Richter, C. Shipboard Scientific Party ODP Leg 160. in *Proceeding of the Ocean Drilling Program, Scientific Results* vol. 160 972 (1996).
3. Emeis, K.-C., Sakamoto, T., Wehausen, R. & Brumsack, H.-J. The sapropel record of the eastern Mediterranean Sea—results of Ocean Drilling Program Leg 160. *Palaeogeogr. Palaeoclimatol. Palaeoecol.* **158**, 371–395 (2000).
4. Grant, K. M. *et al.* A 3 million year index for North African humidity/aridity and the implication of potential pan-African Humid periods. *Quat. Sci. Rev.* **171**, 100–118 (2017).
5. Laskar, J. *et al.* A long-term numerical solution for the insolation quantities of the Earth. *Astron. Astrophys.* **428**, 261–285 (2004).
6. Rose, C., Polissar, P. J., Tierney, J. E., Filley, T. & deMenocal, P. B. Changes in northeast African hydrology and vegetation associated with Pliocene–Pleistocene sapropel cycles. *Philos. Trans. R. Soc. Lond. B Biol. Sci.* **371**, (2016).
7. Westerhold, T. *et al.* An astronomically dated record of Earth's climate and its predictability over the last 66 million years. *Science* **369**, 1383–1387 (2020).
8. Clark, I. & Fritz, P. *Environmental Isotopes in Hydrogeology*. (CRC Press, 2013). doi:10.1201/9781482242911.